Airborne imaging spectrometer measurements of methane releases under turbulent conditions

Manuel Queißer[1*], Kirill Volter[1], Mohd Bilal[1], Igor Mishin[1], Luke Fries[1], David Vilaseca[1], Zhuldyz Darynova[2], Catherine Juery[3], Errico Armandillo[1], Ravil Idrisov[1], Daria Stepanova[1]

[1]AIRMO GmbH, Berlin, Germany

[2]SeaOwl Energy Services, Toronto, Canada

[3]TotalEnergies, R&D, DEMETER Remote Sensing Team, Pau, France

[*]Corresponding author: manuel@airmo.io, Orcid: 0000-0002-2988-428X, Twitter: ManuelQuei

Airborne imaging spectrometer measurements of methane releases under turbulent conditions

Methane plume detection and quantification from airborne and spaceborne platforms offers a promising approach for monitoring localized greenhouse gas emissions. Its performance must be demonstrated under realistic but controlled conditions. An airborne demonstrator of a compact shortwave infrared imaging spectrometer developed for the AIRMO Earth observation mission was therefore evaluated during a single-blinded methane release experiment at the TotalEnergies Anomaly Detection Initiatives (TADI) test facility in Lacq, France. Measurements were conducted over three days in June 2025 at an altitude of ~2050 m above ground level, with controlled release rates ranging from 12.2 to 104.4 kgCH_4/h. Methane plumes, i.e., spatially coherent column averaged enhancements (ΔXCH_4) were detected and corresponding mass fluxes quantified for emission rates ≥54 kg CH_4/h, with occasional detections at 15.2 kgCH_4/h under favourable conditions. The corresponding probability of detection was ~50% overall and ~75% for releases ≥54 kgCH_4/h. Retrieved source locations were typically within ±30 m of the true release point, and plume lengths ranged from ~40 to ~270 m. Radiometric uncertainty and wind speed uncertainty both dominated retrieved fluxes. Using high temporal resolution wind data from an in-situ meteorological station in comparison to ERA5 wind data lead to more accurate (closer to truth) flux retrieval, provided the optimal averaging time window was known. The latter was found to be longer than typical plume residence times. These results provide valuable guidance for the design of future airborne and spaceborne methane monitoring missions, including the AIRMO concept integrating imaging spectroscopy with micro-lidar aerosol profiling.

Word count: main text 9970, supplementary materials 3228

Introduction

Since the pioneering Earth observation (EO) missions with imaging spectrometer payloads able to detect and quantify trace gases in the Troposphere, such as the Global Ozone monitoring instrument (GOME, Burrows et al., 1999), GOME-2 (Callies et al., 2000) and the Scanning Imaging Absorption Spectrometer for Atmospheric Cartography (SCIAMACHY, Noël et al., 2004), a number of satellite missions able to quantify the greenhouse gases (GHG) CH_4 and CO_2 have been launched, including OCO-2 (Crisp et al., 2017) and TROPOMI on Sentinel-5P (Veefkind et al., 2012). By assimilating the resulting GHG concentrations with atmospheric dispersion modeling, GHG mass emission rates (fluxes) and their source location can be retrieved, enabling global top-down quantification of GHG budgets at a regional scale, which can be confronted with bottom-up inventories, such as the Emissions Database for Global Atmospheric Research (EDGAR, Kondo et al., 2015; Zhang et al., 2025).

While these platforms offer global coverage, their pixel resolution, or ground sampling distance (GSD) is relatively coarse (kilometre-scale) compared to anthropogenic gas emanations (Sherwin et al., 2013), and some have a rather long revisit time (16 days for OCO-2, Crisp et al., 2017). Many anthropogenic GHG sources are, therefore, un-detected and un-quantified, leading to gaps in top-down quantification. Over the last 12 years or so, a new generation of satellites-borne imaging spectrometers with sub-kilometre pixel resolution emerged, including EnMAP (Guanter et al., 2015; Roger et al., 2025), EMIT (Thorpe et al., 2023), MethaneSAT (Dandenault et al., 2020; Bukosa et al., 2024) or CarbonMapper (Duren et al., 2025). These platforms mostly target GHG from point emitters, such as at oil and gas facilities, making them capable to quantify GHG directly at the source, at a more regional or even local scale, which helps to increase the granularity of GHG inventories.

Among these new platforms are the first commercial EO missions, such as GHGSat (Chan Miller et al., 2024). AIRMO, is a commercial EO mission aiming to launch a satellite constellation of micro sat class spacecrafts to detect and quantify methane enhancements (plumes, ΔXCH_4) and mass emission rates (fluxes) of point emitters in target mode. It will initially focus on CH_4 emissions from the oil and gas sector. The payload will consist of a combination of a push broom spectrometer and an aerosol lidar. As will be detailed in a separate article, measured aerosol profiles from the lidar are planned to be used to constrain the retrieval forward model, reducing bias of ΔXCH_4.

The present work presents results from the first validation campaign of the airborne demonstrator of the spectrometer sub-system. The campaign took place at the TotalEnergies Anomaly Detection Initiatives (TADI), a test facility in Lacq, France, during a single-blinded controlled release experiment, carried out by TotalEnergies (TE). The objective was to detect and quantify corresponding methane plumes from the release with at least 50% success rate (probability of detection).

The rest of the paper is organised as follows. First, the release experiment, the hardware and the retrieval approach are briefly described. This is followed by a sensitivity analysis. After that, results are presented and discussed, notably the use of two different wind speed data sets, ERA5 from the European Centre for Medium-Range Weather Forecasts (ECMWF) and high temporal resolution wind speed data from an in-situ meteorological station, and their impact on the accuracy of retrieved fluxes.

Material and Methods

Payload and release experiment details

The payload consists of the push broom imaging spectrometer (PB, Figure 1a), inertial measurement unit (IMU), an RGB camera operating in the visual optical spectrum, power supply and a controller

unit. The latter controls the timing of the acquisition and serves as raw data storage for all sensors. The total assembly weight is <15 kg. Figure 1b shows the payload mounted inside the airplane.

Table 1 summarises the key parameters of the PB. The instrument comprises an objective lens, a slit (6 mm x 30 mm), collimation optics, a grating, focusing optics and a InGaAs detector array (512 across track spatial pixels x 640 spectral pixels with 16 µm pixel pitch). All structural components are CNC-machined from 6061-T6 aluminum with precise positional tolerances, base surface flatness tolerances, concentricity and run-out tolerances, ensuring the required structural rigidity, vibration resistance, and minimal thermoelastic deformation. The enclosure provides protection of the optics from stray light, moisture, and dust, while simultaneously addressing detector thermal stabilization through exposed heat sinks.

The PB measures solar radiance spectra reflected off the Earth's surface in the short wave infrared (SWIR) spectral region. The along-track dimension of the hyperspectral image is created as the spectrometer moves parallel to the Earth's surface. The spectral range, dispersed by the grating, encompasses the vibrational-rotational $2\nu_3$ methane band (R-branch around 1645 nm, separated by ~20 cm^{-1} and the Q-branch near 1666 nm) and the $30013 \leftarrow 00001$ CO_2 band.

The IMU sensor has a 50 Hz sampling rate and is used to determine the geolocation and altitude of the spectrometer needed to determine the ground area scanned by the push broom measurement. The RGB camera footage serves to validate the data from the IMU sensor and to filter out cloudy scenes.

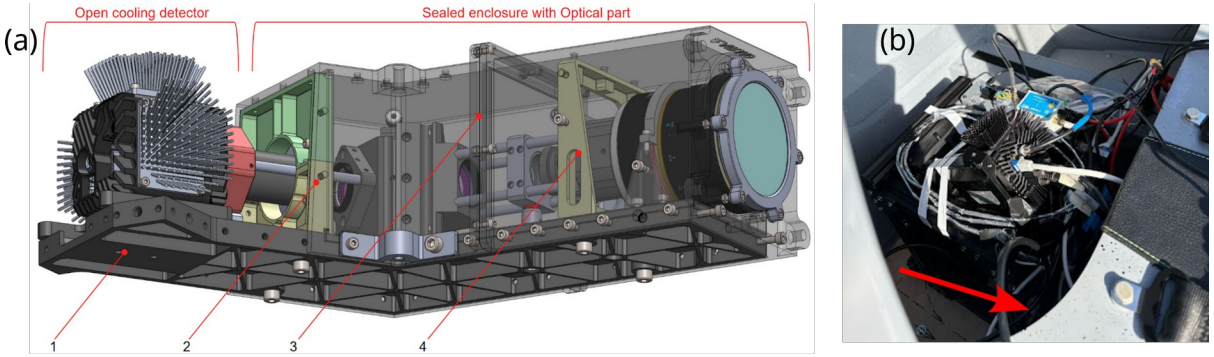

Figure 1. *Payload details. (a) PB spectrometer structure with optical bench (1), rear frame (2), sealed enclosure with protective window (3), and front frame (4). (b) Payload integrated into the aircraft hull. The arrow marks the direction of flight.*

Table 1. *Key characteristics of the push broom spectrometer and payload during the campaign*

Parameter	**Value**
Spectral range	1536 nm - 1670 nm (1594 nm - 1660 nm used for L2)

Grating	600 l/mm
Spectral resolution (FWHM)	0.47 nm
Spectral sampling	~2.2 pixel/FWHM
Field-of-view (FOV) across track	240 mrad
Ground sampling distance (GSD) across track (2000 m altitude)	~0.9 m/px
GSD along track (2000 m altitude)	~8 m/px at 26 m/s ground speed
Power consumption of payload	~30 W
Target detector SNR (albedo 0.3, integration time 0.3 s/px, nadir looking, binning 10 px) at 1660 nm	780
Target column precision CH_4 L2 absolute	< 13 ppb
Target column precision CH_4 L2 relative	< 0.7 %
Target emission rate detection limit (point source)	< 20 $kgCH_4/h$

Controlled methane releases were carried out from 16/06/2025 13:00 to 18/06/2025 13:00 local time at TADI near Lacq, France (Figure 2a). The gas was released at fixed rates of 12.24, 15.2, 54.0, 79.2, and 104.4 $kgCH_4/h$ from a single, fixed location (Figure 2b), which was known to within ~50 m. The release height was 3 m on 16/6 and 17/6 and 1.2 m on 18/6. TE communicated that emission rates were ≥5 $kgCH_4/h$. The actual rates were not disclosed. Except from the first flights on 16/6, when overcast conditions prevailed, the sky was mostly clear (Figure 2c).

87 overpasses were flown in total, with 67 measurement flights and 20 engineering flights. The nominal ground speed was ~26 m/s and altitude 2080 m above ground level (agl, Figure 2d), resulting in a swath (across track foot print) between 400 m and 500 m, depending on the actual altitude. The approximate ground pixel size was 0.9 m (Table 1). The default integration time was 300 ms per frame. For the last flights on 18/6, 400 ms were used.

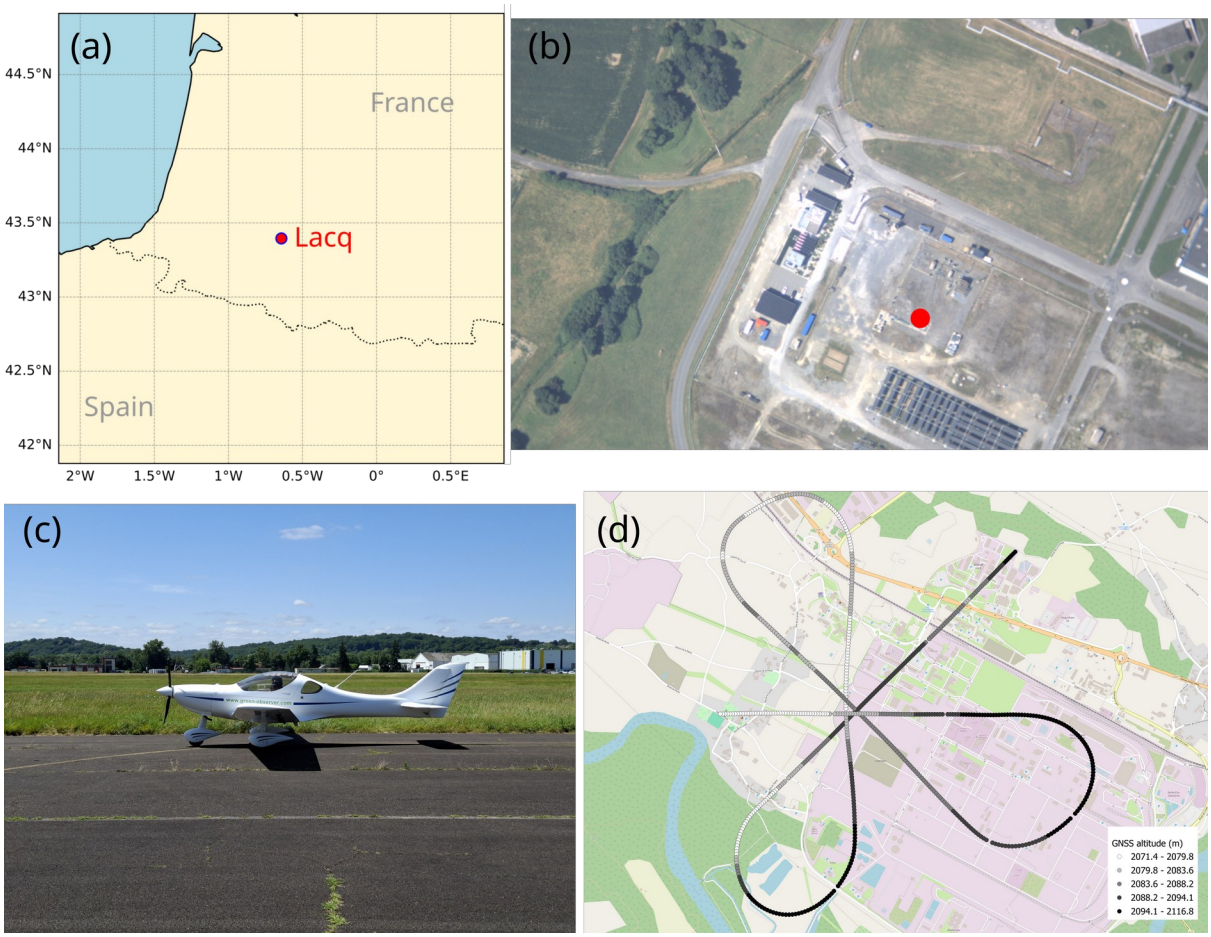

Figure 2. *Release experiment situation. (a) Location of TADI in Southwestern France. (b) Aerial photo from the payload camera (North is along the y-axis). The red dot marks the true location of the release pad. (c) View of the aircraft before take-off on 16/6/2025 12:25 local time. (d) Typical flight pattern, example from 16/6/2025 with altitude. The dots represent the location of the centre of each push broom frame projected to the ground. The release pad is near the crossing point.*

Data processing

A brief description of the end-to-end processing pipeline (E2E) is given in the following. A more detailed description can be found in the supplementary material.

The E2E also functions as an end-to-end simulator to assess performance and specifications of the spectrometer. Raw frames within a certain radius around the area of interest were selected, i.e., the release site near the crossing point of the flight legs (Figure 2d), corresponding to a duration of around 20 s per overpass. From these frames, raw spectra (Level-0, L0 data) were pre-processed into geolocated, instrument corrected spectra (Level 1b, L1b). To that end, a set of calibration key data was used (supplementary material S1), which includes wavelength calibration, pixel response non-uniformity (PRNU) correction and the instrumental spectral response function (ISRF).

To enhance signal-to-noise ratio (SNR) of the spectra, for each frame, across track pixels were binned. Plume dilution, that is, ground pixels that were only partly covered by methane enhancements, was to be minimized. As a compromise, a pixel binning of 10 was applied, which entails ~9 m ground sampling distance (GSD) across track (Table 1). No grouping was applied, resulting in ~8 m GSD along track. This corresponds to almost a square pixel, which was deemed beneficial for geolocalization using the IMU data.

In the Level-2 processing, for each binned pixel, and for each altitude layer j, an initial guess of layer-integrated column density $VCD_{i,j}$ (in molec.cm^{-2}) for dry air and atmospheric trace gases $i \in$ [XCH_4, XCO_2, XH_2O] is created. For each pixel, an iterative Levenberg-Marquardt scheme minimizes the misfit between L1b and a forward modeled spectrum from a non-scattering radiative transfer model between 1594 nm and 1660 nm, thereby updating $VCD_{i,j}$. To arrive at Level-2 results (XCH_4 images), for each pixel, dry air mole fractions (column averaged mixing ratios) are computed from the final updated $VCD_{i,j}$ as

$$X_i = \frac{\sum_{j}^{nlays} VCD_{i,j}}{\sum_{j}^{nlays} VCD_{air,j}} \quad (1)$$

Additionally, to correct for surface related artifacts and for aerosol scattering, including multiple scattering (e.g., between surface and aerosols), XCH_4 was retrieved using the proven CO_2-proxy method (Frankenberg et al., 2005b; Krings et al., 2011; Chan Miller et al., 2024). The principle of the proxy method is that the effect of scattering cancels out by scaling the methane VCD with the proxy gas mixing ratio to VCD ratio, which can be written as

$$X_{CH_4} = \frac{X_{CH_4}}{X_{CO_2}} XCO_{2,av}\,, \quad (2)$$

where XCO_2 and XCH_4 were obtained from Equation (1). $XCO_{2,av}$ is the climatological mean of the CO_2 mixing ratio over the sounding area.

To obtain column averaged CH_4 enhancements (Level-3, L3), a plume detection algorithm based on a z-test was applied to the XCH_4 images (supplementary materials, S3.3). This results in a plume mask, which depicts plume pixels.

Level-4 (L4) products, i.e., methane mass emission rate (flux), were retrieved using the integrated mass enhancement (IME) method (Frankenberg et al., 2016; Varon et al., 2018):

$$\phi = \frac{u_{eff}}{l} IME \quad (3)$$

where ϕ is the CH_4 flux (in kg/s), IME is the integrated mass enhancement, calculated as the sum over the N plume pixels as

$$IME = \frac{M}{N_A} \sum_{i}^{N} \Delta XCH_{4,i} VCD_{air,i} A_i, \quad (4)$$

where $\Delta XCH_{4,i}$ is the enhancement of methane volume mixing ratio, calculated as

$$\Delta XCH_{4,i} = XCH_{4,plume,i} - XCH_{4,bg} \quad (5)$$

where $XCH_{4,plume,i}$ is the methane mixing ratio for plume pixel i and $XCH_{4,bg}$ for the background, calculated using a local median filter (Varon et al., 2018). M is the methane molar mass (kg/mol), N_A is Avogadro's number (molec/mol), $VCD_{air,i}$ is the dry air column density (molec/m^2) derived from ERA5 air pressure and humidity profiles (more details in supplementary materials, section S2.2). A_i is the ground surface area of the geolocated plume pixel i. l is the plume length, derived as the square root of the plume mask area (Bruno et al., 2024). u_{eff} is the effective wind speed (plume speed), corresponding to the rate of turbulent diffusion.

The IME method assumes a constant emission rate during the overpass and that the plume integrated methane mass is related to the emission rate by the residence time $t_{res} = l/u_{eff}$, which represents the time before methane is dispersed to a concentration that can no longer be resolved by the instrument. Varon et al. (2018) retrieved u_{eff} by simulating flux retrievals for many random plumes from large eddy simulation (LES). For a range of given 10 m wind speeds u_{10} they were solving Equation (3) for u_{eff}, and fitted it to u_{10} with $u_{eff} = a_1 \log_{10} u_{10} + a_2$. $a_1$and a_2 depend on instrument precision. Accordingly, we use this relationship to calculate u_{eff} from u_{10}, adopting 0.9 and 0.6 for a_1 and a_2, respectively.

The L4 uncertainty is estimated using Gaussian error propagation of Equation (3), assuming uncorrelated errors, as

$$\sigma_\phi = \sqrt{{\sigma_u}^2 + {\sigma_{\Delta XCH_4}}^2 + {\sigma_{VCD}}^2}. \quad (6)$$

σ_ϕ is the flux uncertainty (1 standard deviation, STD in kgCH_4/h), σ_u is the flux uncertainty attributed to the effective wind speed (i.e., plume speed). $\sigma_{\Delta XCH_4}$ is the flux uncertainty from the methane enhancement uncertainty (radiometric contribution) and σ_{VCD} is the flux uncertainty caused by the uncertainty of the dry air column density. These contributions are further detailed in the supplementary materials, section S2.4. There, the impact of the correlation of l with IME on the uncertainty is assessed using Monte Carlo analysis.

Wind data

Initially, we retrieved u_{10} from the ERA5 land product. The data set has ~0.1° (~9 km) spatial resolution and 1 h temporal resolution. The data point closest to the centre of the swath was chosen. A fixed uncertainty of 0.21 m/s was assumed (Giusti, 2022), representing the combined effects of model

and representation errors at the spatial and temporal resolution of the ERA5 data.

Upon de-blinding the L4 results, TE shared wind data with 5s temporal resolution from a meteorological station (MS), installed at 1.5 m agl near the release pad, consisting of horizontal wind speed and wind direction. They were deemed more representative than ERA5 wind data. Therefore, the MS wind speeds were adopted as u_{10} and used to recompute fluxes to assess whether this would improve their accuracy.

Figure 3 shows both wind data sets. Wind captured by the MS reveals a high degree of variability over the course of an hour. Over larger time scales, wind speeds from ERA5 are fairly in line with the MS readings, but ERA5 slightly underestimates the MS wind speeds with 1.2 m/s and 1.5 m/s mean values over all overpasses from ERA5 and MS, respectively. While the 16/6 was characterised by medium wind speeds (2.5 to 3 m/s), on 17/6 and 18/6 relatively low wind speeds prevailed (~2.9 m/s peak), which were highly variable in velocity and direction.

Large structures around the TADI site with hills south of it caused a more complex wind field. For all 3 days, surface sensible upward heat flux retrieved from ERA5 land increased from ~30 W/m² at noon to ~90 W/m² in the late afternoon. This indicates moderate surface heating and associated buoyancy fluxes, which likely contributed to the development of a weakly to moderately convective boundary layer, particularly during the afternoon measurements of the first two days (Figure 3). In real operations, these times of the days, especially during summer, would thus be less favorable for plume quantification (Wolff et al., 2021). These conditions were accompanied by friction velocities around 0.15 m/s (Figure 3). Using ERA5 2m temperature as a proxy for potential temperature (~295 K in late afternoon), this corresponds to Monin-Obukhov lengths of approximately -10 m, indicating unstable, buoyancy-dominated conditions. This is in line with rapid speed and direction changes observed during most of the ~20 s overpasses on the first two days, e.g. at 16:28 on 17/6, when wind speed changed from 1.5 to 2.5 m/s and wind direction by tens of degrees. For the overpasses on 17/6 (Figure 3, 16:20-17:00), turbulence indices (wind speed STD/mean) were up to 0.5. Measurements on 18/6 were conducted close to noon and exhibited relatively low friction velocities (~0.06 m/s), suggesting weaker mechanical turbulence, but convectively unstable conditions (Monin-Obukhov length around -1 m).

To account for temporal variability, u_{eff} was calculated from the average u_{10}. The latter was calculated as the vector mean of the instantaneous velocity components as

$$u_{10}=\sqrt{\bar{u}^2+\bar{v}^2}, \quad (7)$$

with $\bar{u}=\frac{1}{S}\sum u_i$, $u_i=U_i\cos\theta_i$ and $\bar{v}=\frac{1}{S}\sum v_i$, $v_i=U_i\sin\theta_i$, where S is the number of 5s samples in the averaging time window. The wind speed uncertainty was estimated as the STD of the projected magnitude of u_i and v_i onto the mean wind direction within the averaging time window:

$$STD\left(\left| u_i\cos\theta_{mean}+v_i\sin\theta_{mean}\right|\right), \quad (8)$$

with $\theta_{mean} = \tan^{-1}(\bar{v}/\bar{u})$. To estimate the averaging time window, for each individual overpass an iterative scheme was used similar to Varon et al. (2018). The averaging time was recursively increased until u_{eff} stabilised (change <1%).

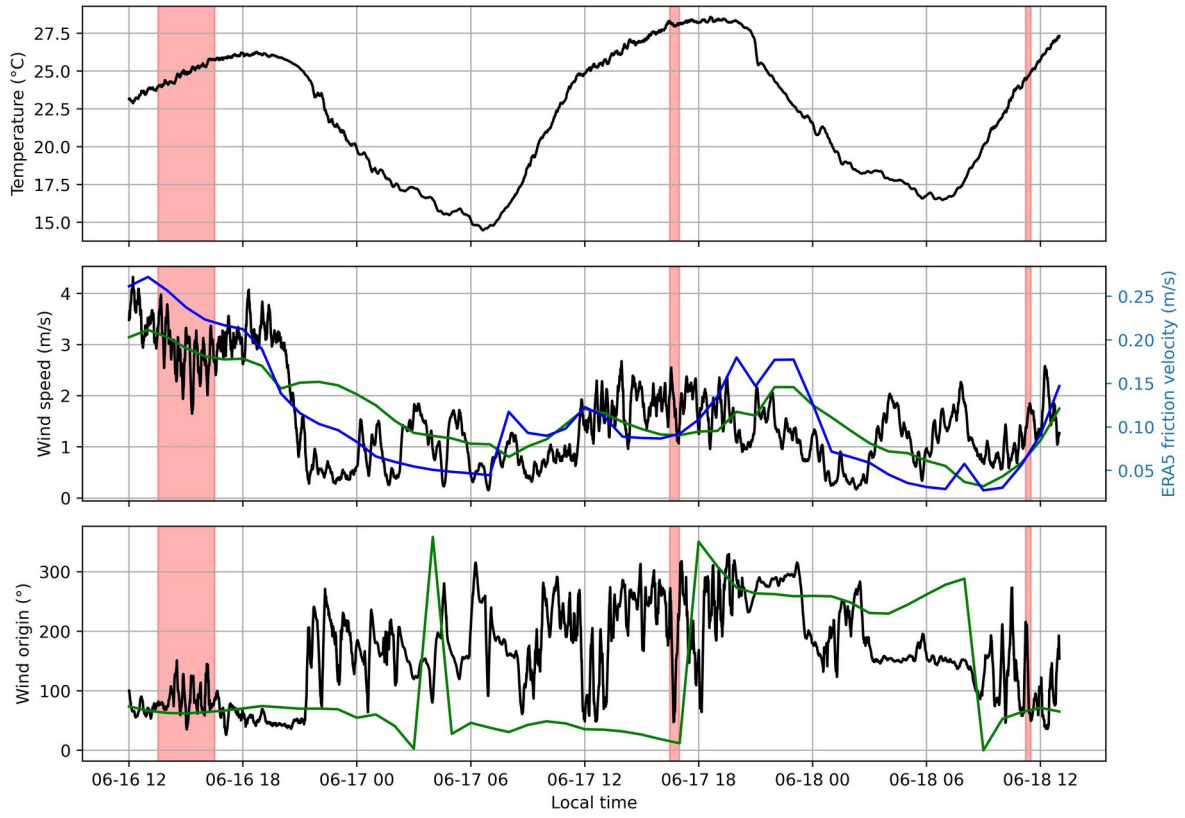

Figure 3. *Meteorological data for 16/6 to 18/6/2025 at Lacq, France.* Temperatures *from the in-situ meteorological station, friction velocity from ERA5 reanalysis data (blue). Wind speed and direction from MS (black) and ERA5 land (green). A 10-minutes moving average has been applied to the MS data for display purposes, which smoothed out high frequency variations. The red boxes highlight periods when all results presented in this paper were acquired.*

Sensitivity estimation

What would be the smallest detectable CH_4 enhancement and emission rate (flux) during the campaign? To answer this question before the campaign, a sensitivity estimation was carried out.

First, using the E2E in simulation mode, the instrument SNR for the expected observation geometries was computed. The SNR is governed mainly by solar zenith angle (SZA) and the local ground albedo (0.05 up to 0.4, typically ~0.18 as derived from Sentinel-2 data). With a pixel binning of 10 and SZA ~40°, albedo ≤0.3, the expected SNR are between ~100 and ~600 (Figure 4).

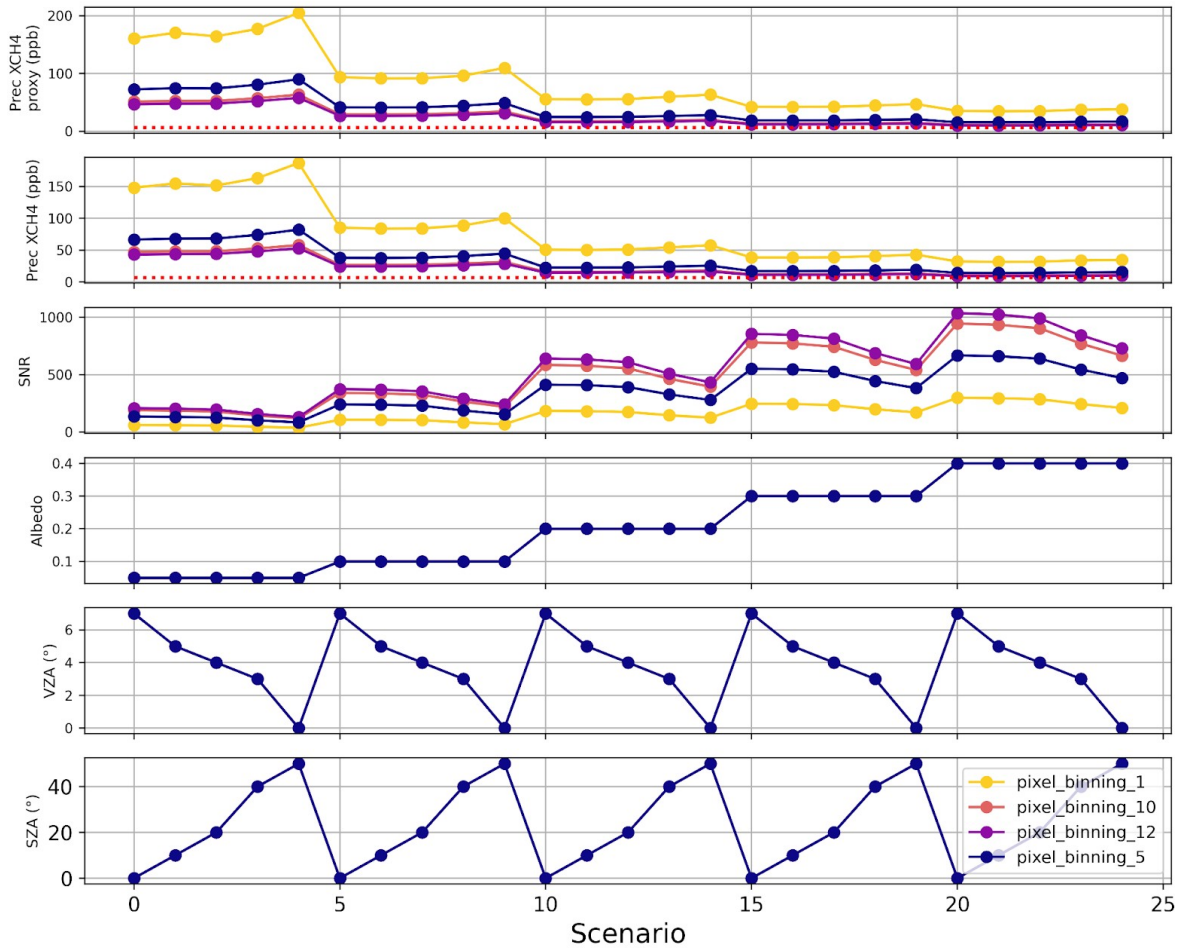

Figure 4. *Simulation results for a single pixel scenario using the push broom spectrometer settings for this campaign assuming a flight altitude of 2000 m. Level-2 results, including precision (1 STD), SNR for different observation scenarios. Red dots mark 7 ppb, estimated to be the minimum precision to detect a flux of 5 kgCH_4/h. Prec depicts XCH_4 precision retrieved from the fit covariance matrix.*

To relate SNR to minimum detectable flux, a first order slab mass balance model is used (Gerilowski et al. 2011; Jacob et al., 2020). To that end, Equation (3) is simplified by assuming a rectangular plume footprint equaling a single spectrometer pixel corresponding to the total plume area, with equal enhancement across the plume, so that $\sum_i^N \Delta VCD_i A_i \approx \Delta VCD \sum_i^N A_i$,

with $\Delta VCD = \Delta XCH_4 VCD_{air}$. VCD_{air} is the dry air total vertical column density. The flux is approximated as

$$\phi \approx u_{eff} \frac{M}{N_A} \frac{\Delta VCD}{VCD} VCD\, w, \qquad (9)$$

where ΔVCD is the methane column enhancement and VCD is the methane total vertical column density (both in molec.m^{-2}), w is the plume width. The plume length l cancels out, since surface area

covered by the column enhancement is assumed to equal the plume area, $wl = \sum_{i}^{N} A_i$. Assuming linearity between optical depth and VCD, using basic signal processing theory and the Beer-Lambert law, and assuming

$$\frac{\Delta VCD}{VCD} \approx \frac{1}{SNR\,\sigma(\lambda)\,VCD}, \tag{10}$$

that is, detection limit (noise limit) of the relative column enhancement $\frac{\Delta VCD}{VCD}$, we arrive at a minimum detectable flux of

$$\phi \approx u_{eff} \frac{1}{SNR\,\sigma(\lambda)} \frac{M}{N_A} w, \tag{11}$$

where $\sigma(\lambda)$ is the methane absorption cross section, for which an approximate value of ~0.6×10^{-24} m^2 is adopted (averaged over absorption lines between 1630 nm and 1660 nm), M is the methane molar mass, N_A is Avogadro's number.

Since the flux was unknown, a reasonable plume dimension of w=20 m was adopted, as observed in similar campaigns (e.g., Chulakadabba et al., 2023). Assuming a reasonable u_{eff}= 2 m/s, Equation (11) yields a minimum detectable flux of ~64 $kgCH_4/h$ and ~11 $kgCH_4/h$ for SNR of 100 and ~600, respectively (best case). If the plume was diluted over a width of w=40 m, these numbers would be twice as high, and so on. This SNR only takes into account observation conditions and the instrument model, but no other sources of error, e.g., instrument errors, that would lead to a lower posterior SNR (retrieval SNR), which makes this an optimistic estimate.

For experimental evidence, the push broom spectrometer was set up in a sun illuminated target geometry, staring at a tree in ~15 m distance. 10 cm long calibration cells, each pre-filled with different fixed XCH_4, were mounted in front of the spectrometer entrance window. The cells contained a corresponding CH_4 column amount of 33 ppm.m, 120 ppm.m, and 2400 ppm.m, respectively. A reference measurement without cell (0 ppm.m enhancement) was done. For each cell, a number of >10 frames were acquired and processed into L2 (XCH_4 pseudo scene) using the same pipeline as for the airborne measurements, including the 10-fold pixel binning. Scene mean XCH_4, standard error of the scene mean, and p-values from a two sample Welch's t-test were computed for each pseudo scene. Standard errors of the scene mean ranged between 12 and 23 $ppbCH_4$. For enhancements ≥120 ppm.m, standard errors were smaller than the increase in scene mean and p-values were < 0.05. Both metrics indicate a statistically significant increase in measured enhancement, suggesting that, and depending on the observation conditions, the PB would in principle be capable of resolving enhancements of 120 ppm.m or ~0.8% of ambient methane mixing ratios.

Assuming the minimum expected release rate of ϕ=5 $kgCH_4/h$, a typical atmospheric methane VCD of ~3.8×10^{23} $molec.m^{-2}$, Equation (9) yields an expected relative column enhancement $\frac{\Delta VCD}{VCD}$

of only ~0.4% (or ~7 ppb, red dotted line in Figure 4), suggesting that fluxes this low would not be detectable. The experiment was repeated several times using a different sun illuminated target with the same outcome.

Results and Discussion

The actual observed sensitivity per spectrometer pixel was computed as the mean intensity of the spectrum over the standard deviation of the fit residuals (Gerilowski et al., 2011) and ranged between 100 and 170 (Figure 5), strongly dependent on SZA and albedo. Note that this SNR, unlike the instrument SNR (Table 1, Figure 4), accounts for all sources of uncertainty in the processing chain, including detector related sources (e.g., observation conditions), instrument errors (e.g., stray light), atmospheric contributions (e.g., aerosol and cloud scattering), and model errors (e.g., deviations from Lambertian scattering, errors in solar reference spectrum). SZA during the overpasses ranged from 20° to 42°. Lowest fit residuals, associated with largest SNR ($\geq$150) were retrieved for lowest SZA (around mid-day). SNR were lower for higher SZA during afternoon (~120). For a given overpass, SNR also varied by up to ~40% due to fluctuations in surface reflectivity along the flight track.

Using Equation (10) with SNR 140, the estimated detection limit is ~$1/(140 \times 0.6 \times 10^{-24}$ m^2) or ~1.2×10^{22} molec.m^{-2}, or ~3% of ambient methane levels, i.e., ~60 ppb. This is in line with the covariance matrix derived XCH_4 precision (Equation (S6)), which varied between 68 and 90 ppb for different overpasses (mean over plume delineated area). The associated precision for CO_2 varied between 16 and 22 ppm. The corresponding estimated detection limit for methane relative to the total atmospheric column is ~630 ppm.m, and ~500 ppm.m, in good conditions, that is, for SNR ≥140, albedo >0.2, solar zenith angle <30°. Adopting the slab model (Equation (11)), assuming u_{eff}=2 m/s and w=20 m, this corresponds to a minimum detectable flux of ~46 kgCH_4/h.

The retrieval also yielded relative surface reflectance (supplementary material S2.2). An example is shown in Figure 6. It was used to visually and qualitatively assess the goodness of the fit for the complete scene. That means, if the relative distribution of the surface reflectance is in line with the ground truth from the visual camera, this indicates convergence to the global minimum. Obvious artifacts in the reflectance image, on the other hand, would indicate falsely attributed trace gas optical density changes and hence erroneous XCH_4.

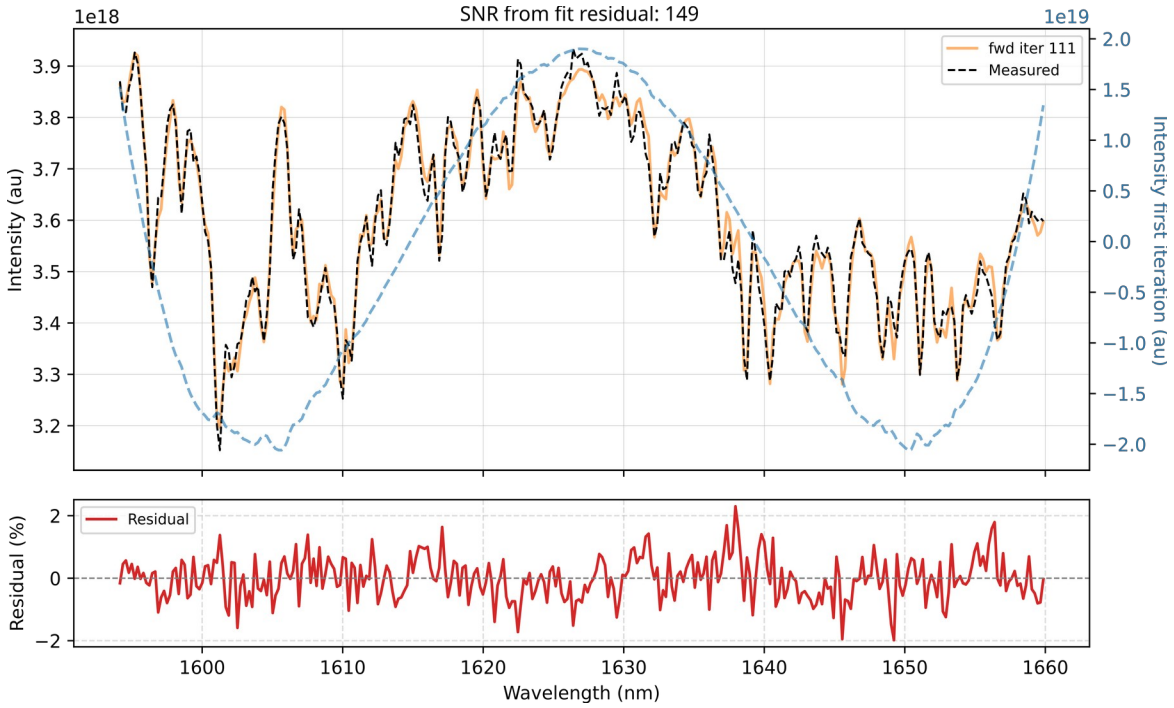

Figure 5. *Typical measured radiance spectrum for a single pixel. Shown is the measured L1b spectrum (black dotted) and the first (blue) and final iteration (orange) of the forward modeled radiance spectrum and the final fit residuals below.*

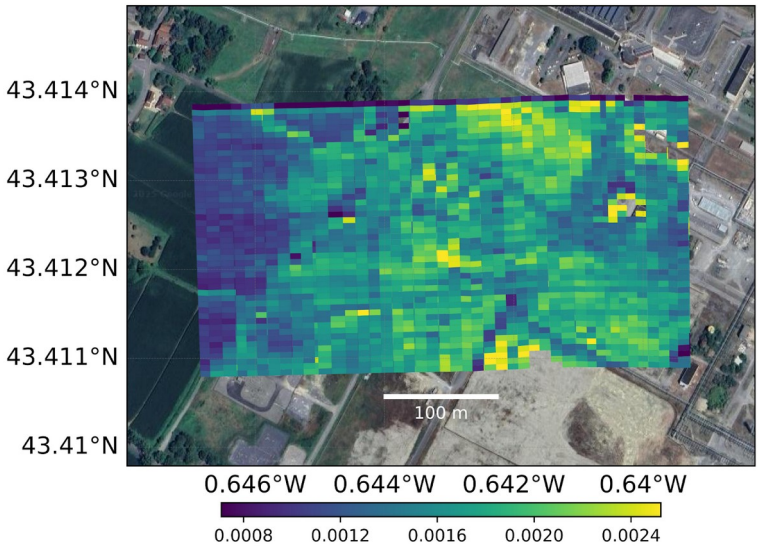

Figure 6. *Example of retrieved relative ground reflectance at the release site from one of the overpasses on 17/6/2025. No orthorectification was applied and the albedo image has not been projected onto a map, which may cause it to be spatially distorted near the edges. Base photo data: Google tiles API.*

Table 2 lists all overpasses with their respective ID for which a L2 XCH_4 image with a plume could be detected. Figure 7 shows a XCH_4 image for overpass 904-950 from 16/6/2025, during the release of 104.4 kg CH_4/h. The overpass lasted 16 s. Also shown are the proxy-based XCH_4 (Equation (2)). Since XCO_2 acts as a light path proxy, effects such as path shortening related to aerosols or surface scattering common to both CO_2 and CH_4 spectral regions theoretically cancel out. This is indeed suggested by the "cleaner" XCH_4 image (Figure 7c). Lowest RMS errors (best fits) are achieved over bright terrain (gravel, concrete) around the release site, whilst poorest fits are retrieved for pixels over low albedo areas, such as the woods at the edges of the swath, in the northwestern corner of the scene (Figures 7b and d).

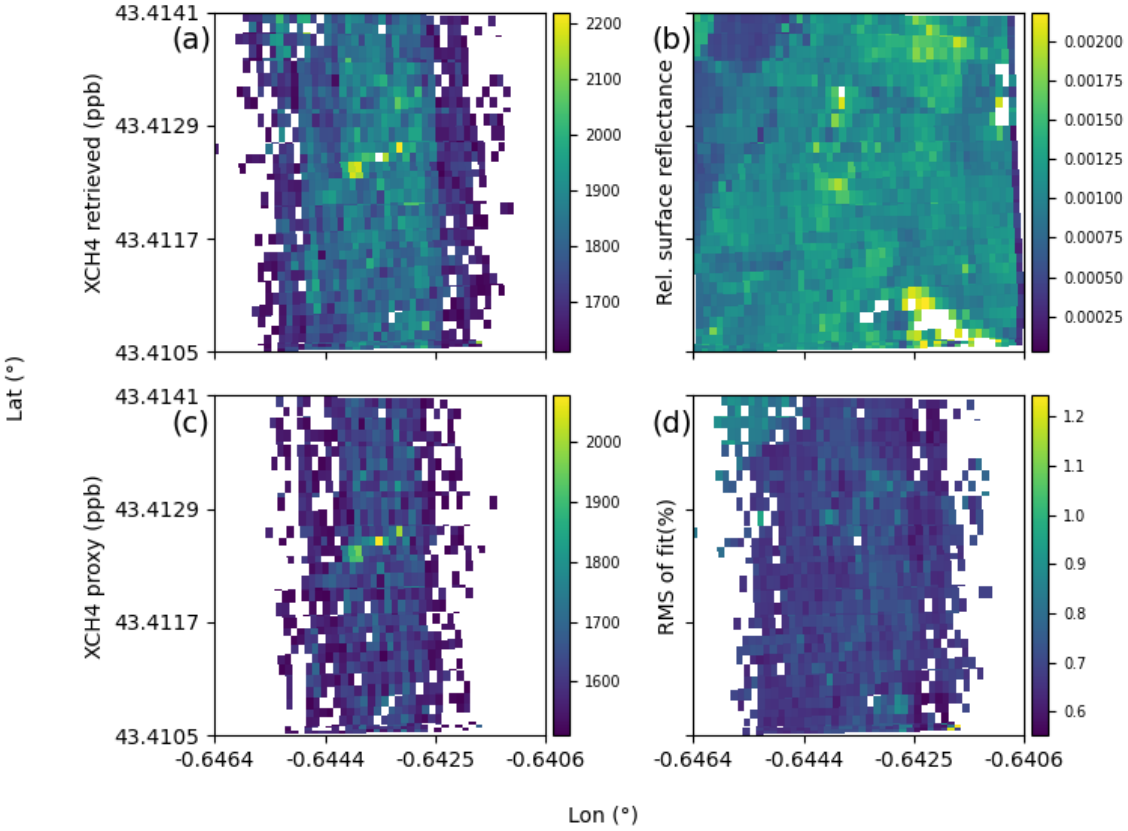

Figure 7. *L2 Result for overpass 904-950 on 16/6/2025 at 13:48 local time. (a) XCH_4 from direct retrieval. (b) Retrieved relative surface reflectance. (c) XCH_4 from proxy. (d) RMS fitting error. Flight heading is ~180°, i.e., south. Pixels are plotted with coordinates from the IMU.*

The mean precision over the plume pixels is 87 ppb for CH_4 and 23 ppm for CO_2, and the mean proxy precision is 116 ppb. The mean XCH_4 over the scene is 1829 ppb (proxy 1590 ppb), indicating a significant negative bias. The latter is observed in both the direct and proxy XCH_4 for all overpasses. For instance, on 17 June, mean scene-averaged XCH_4 values are 1752 ppb (direct) and

1626 ppb (proxy). The cause is currently under investigation. The bias persists even in the proxy XCH_4 retrieval, which suggests non-atmospheric or surface-related contributions. No significant correlation was found between the directly retrieved XCH_4 and the solar zenith angle (Pearson cross correlation coefficient r = 0.01) or azimuth angle (r = 0.28) for any of the three flight days, suggesting that aerosol scattering did not have a major effect on the observed bias. This is consistent with previous work (Thompson et al., 2015), which showed that at low flight altitudes, aerosol scattering effects are considerably weaker than for space-borne spectrometers.

XCO_2 are overestimated for most, but not all overpasses, with mean XCO_2 of 449.8 ppm (mean over plume and over overpasses for 17/6/2025) compared with the mean XCO_2 in the area and during the three days of the campaign of ~427 ppm, as retrieved from OCO-2 data. The latter is used as the climatological background XCO_2 for the proxy method. This discrepancy (~5 %), is in line with the ~6% difference between proxy and direct XCH_4. Possible causes include: overfitting due to contribution of spatial stray light, or an incomplete characterization of the instrumental response function (ISRF). Dedicated tests using out-of-band light sources did not indicate out-of-band stray light contamination.

For the data processing, the bias is assumed to be spatially constant, so that the L3 product (XCH_4 enhancements) would not be affected, since the bias would cancel when computing the difference between plume and background XCH_4.

In addition, an approximately circular bias is evident for all L2 results, increasing with distance from the swath centre. The reason for this is currently under study and might be related to an imperfect correction of the smile effect (an optical distortion, supplementary materials S2). However, enhancements are detected in the centre region of the swath, where the circular bias is approximately flat. This bias is, therefore, deemed to have an insignificant effect on the largest enhancement, which are located at the swath centre pixels. The effect is even smaller for the plume edge pixels, since the corresponding CH_4 enhancements are lower and therefore contribute little to the IME. This was verified by applying a flattening of the circular bias by fitting it with a polynomial for each along-track pixel.

Figure 8 shows diagnostic output from the L2 retrieval. The measured L1b spectra contain no information on the vertical distribution of air and trace gas molecules and the retrieved L2 trace gas mixing ratios, such as XCH_4, are column averaged. However, given by the measurement geometry and the air pressure profile, most methane molecules are situated in the planetary boundary layer, just under the aircraft altitude. Hence, a change in modeled optical density near the surface would cause the largest change in forward modeled spectral intensity, i.e., retrieval sensitivity is highest. This is quantified by the column averaging kernel (AK, Figure 8a). Since sunlight passes the air column below the aircraft twice before reaching the spectrometer, the retrieval sensitivity is roughly twice as high for the altitude below the aircraft compared to just above the aircraft. Figure 8b shows the Jacobian for methane for the total column for a selected pixel, which shows the sensitivity of the

forward modeled radiance to a change in optical density in the wavelength range used for the L2 retrieval.

Table 2. *Overview of the measurement flight acquisitions with overpass leg ID (corresponding to a single leg of a star pattern such as depicted in Figure 2d) and releases and Level 4 estimates (methane fluxes) using wind speeds from ECMWF ERA5 and the local meteorological station (MS). Times are local (UTC + 2h). Flux uncertainty estimates are 1 standard deviation (STD). Only overpasses of measurement flights and with detected plumes are shown. Integration time was 400 ms for flight fc7ab0fd on 18/6 and 300 ms for all other flights. For overpasses 602-642 and 32-91, both 16/6, there are likely missing plume pixels. WD is wind direction. Overpasses in the plots are marked bold.*

Date	**Overpass ID**	**Local start time**	**Flight overpass ID**	u_{eff} **(m/s) ERA 5**	u_{eff} **(m/s) MS**	**WD (°) ERA 5**	**WD** (θ_{mean}) **(°) MS**	**True release rate (kg/h)**	**L4 Flux estimate ERA5 (kg/h)**	**L4 Flux estimate MS (kg/h)**	**Plume length retrieved (m)**
16/6	866-927	13:31	d2d815dc	1.7	1.8	66	76	104.4	87 ± 25	91 ± 31	126
	30-84	13:44	5d81f544	1.7	1.8	66	85	104.4	85 ± 36	89 ± 62	60
	310-374	13:45	5d81f544	1.7	1.6	66	80	104.4	110 ± 48	107 ± 87	95
	602-642	13:47	5d81f544	1.7	1.6	66	70	104.4	46 ± 30	43 ± 30	20
	904-950	**13:48**	**5d81f544**	**1.7**	**1.6**	**66**	**80**	**104.4**	**160 ± 39**	**155 ± 114**	**82**
	58-124	13:59	d3dddedd	1.7	2.1	66	80	104.4	107 ± 32	132 ± 39	72
	349-398	14:01	d3dddedd	1.6	1.6	65	90	104.4	359 ± 44	344 ± 40	108
	32-91	14:10	a5389296	3.1	1.8	64	65	104.4	47 ± 27	91 ± 31	28
	608-710	16:29	16196825	2.8	1.7	96	61	54.0	92 ± 40	101 ± 52	75
	960-1014	16:31	16196825	2.8	1.4	62	62	54.0	37 ± 29	34 ± 37	42
17/6	554-618	16:28	90224c3c	0.7	1.1	3	11	79.20	90 ± 34	137 ± 107	90
	1349-1409	16:32	90224c3c	0.7	1.6	2	324	79.20	45 ± 22	95 ± 30	60
	1637-1707	16:34	90224c3c	0.7	1.4	3	334	79.20	39 ± 18	75 ± 45	66
	1894-1977	16:35	90224c3c	0.7	1.3	2	19	79.20	50 ± 16	89 ± 34	187
	2214-2279	16:37	90224c3c	0.7	1.1	3	27	79.20	62 ± 22	97 ± 36	72
	2744-2795	16:40	90224c3c	0.7	0.7	2	357	79.20	59 ± 17	55 ± 75	162
	3000-3060	**16:42**	**90224c3c**	**0.7**	**1.2**	**3**	**65**	**79.20**	**61 ± 23**	**96 ± 49**	**94**
	3230-3342	16:43	90224c3c	0.7	1.1	2	74	79.20	76 ± 24	112 ± 37	78
	3503-3594	16:44	90224c3c	0.7	1.1	2	34	79.20	63 ± 16	96 ± 42	274
	3810-3872	16:46	90224c3c	0.7	1.0	2	26	79.20	48 ± 19	67 ± 55	60
	4088-4155	16:48	90224c3c	0.7	0.2	2	24	79.20	34 ± 14	9 ± 14	51
	4365-4434	16:49	90224c3c	0.7	0.5	3	41	79.20	74 ± 22	50 ± 27	90
	4613-4698	16:50	90224c3c	0.7	1.7	2	344	79.20	72 ± 22	141 ± 36	149
	5069-5133	16:53	90224c3c	0.7	0.3	3	312	79.20	39 ± 15	16 ± 8	87

	5342-5403	16:54	90224c3c	0.7	0.5	2	81	79.20	115 ± 31	79 ± 61	55
	5627-5693	16:56	90224c3c	0.7	0.4	3	345	79.20	85 ± 24	49 ± 81	158
	5903-5960	16:58	90224c3c	0.7	0.3	2	342	79.20	68 ± 22	26 ± 59	84
18/6	**2367-2463**	**11:13**	**ac39934b**	**0.2**	**0.8**	**64**	**343**	**15.20**	**11 ± 10**	**30 ± 19**	**60**
	4331-4395	11:24	ac39934b	0.2	1.3	64	74	15.20	8 ± 7	38 ± 24	48
	39-76	11:30	fc7ab0fd	0.2	0.8	64	50	15.20	10 ± 10	30 ± 27	60

Figure 7 (a) and in particular the proxy result in Figure 7 (c) suggests a coherent enhancement feature in the middle of the swath, in line with the dominant wind direction at 14:00 local time (ENE), commencing approximately above the supposed release site.

Before computing from the L2 result the L3 product, i.e., the plume mask and enhancements (in ppb), a threshold filtering was applied for each pixel (L2 RMS fit residuals < 1.4). For all scenes that were classified as containing a potential plume, such as in Fig. 7, it was verified that enhancements were actually caused by CH_4, and were not false positives, e.g., due to interfering surface features, using the following procedure. First, a visual assessment verified that the source location of each potential plume (i.e. the detected plume mask) would be near the suspected source location, and that it was uncorrelated with visible surface features or changes in albedo. In addition, mean L1b radiance spectra inside and outside the detected plume mask were compared, confirming reduced average transmission along the methane spectral band for the retrieved plume pixels (Figure 8c).

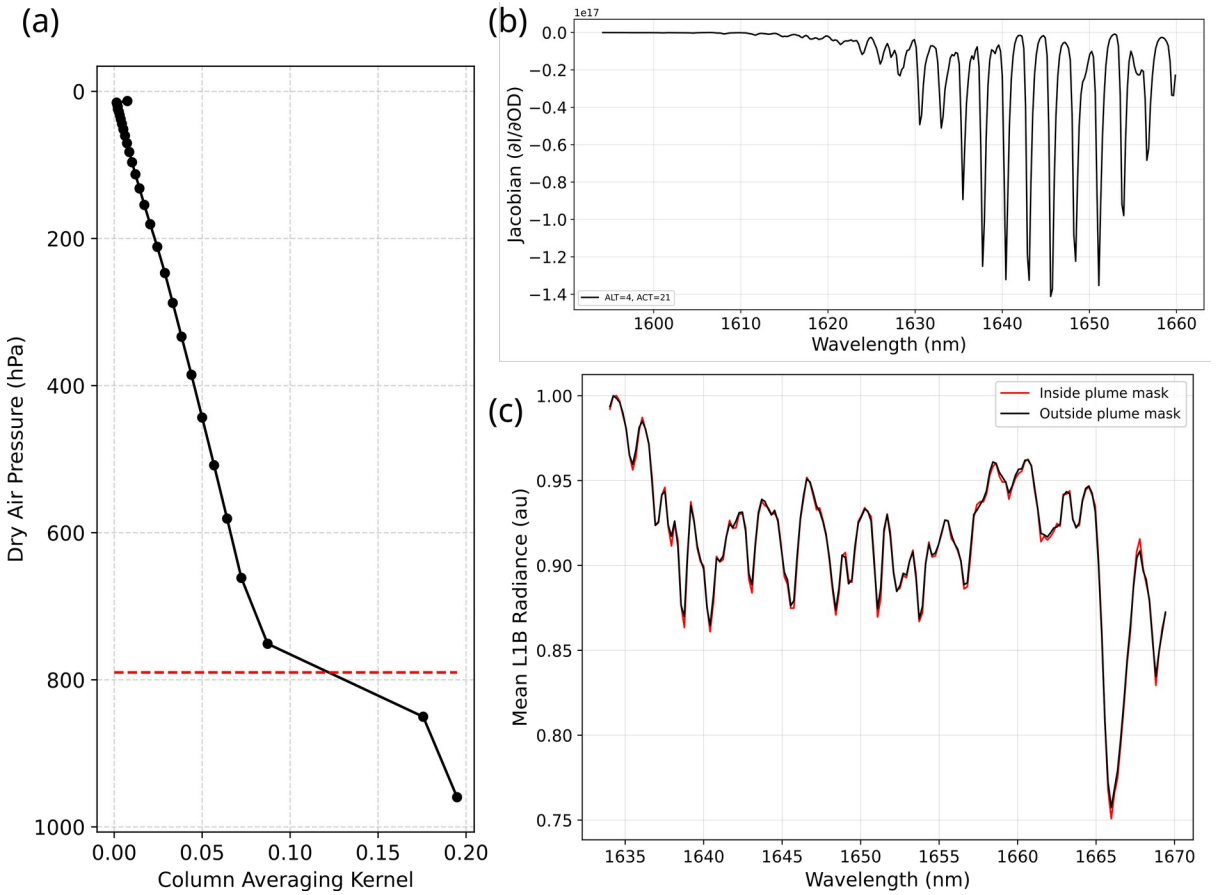

Figure 8. *Diagnostics for overpass 904-950 (Figure 7). (a) Column averaging kernel for all 30 height layers displaying the fractional distribution of retrieval sensitivity across the 30 vertical model layers (mean over scene). The averaging kernel is normalised by the sum (Rodgers, 2000). The aircraft altitude at ca. 790 hPa is depicted by the red dotted line. (b) Total column Jacobian (derivative of spectral intensity with respect to optical density, OD) for methane for along track pixel 4 and across track pixel 21 (centre swath). (c) Mean L1b spectra with the main methane absorption features.*

Figure 9 shows the process of plume delineation and the L3 plume mask results for the L2 result for overpass 904-950 (Figure 7). Figure 9d depicts the final masked plume enhancements projected onto an aerial photo of the release site. The retrieved plume commences ~16 m from the source location. The retrieved source location (highest enhancement) is ~30 m (~3 pixels) away from the true source location. This could be attributed to XCH_4 noise or the lack of orthorectification associated with an imperfect aircraft pitch angle correction (< 10 m offset). In addition, physical mechanisms, such as plume dilution may have contributed. The binned pixel of ~8 m x 9 m nearest to the source may have only partly been covered by the plume. Furthermore, dispersion processes on a sub-pixel scale may have caused maximum enhancements not to coincide with the pixel at the release pad at the time of acquisition.

Figure 10a shows the L3 result (delineated methane enhancement) from 17/6/2025 for

overpass 3000-3060 during a release rate of 79.2 kgCH_4/h (Table 2). The retrieved source location is just ~10 m north of the true source location.

The lowest flux of 12.4 kgCH_4/h was released on 16/6 14:13 to 15:00 local time. Coherent with the sensitivity estimation above, no plume enhancements could be detected for this release rate. For the second lowest emission rate of 15.12 kgCH_4/h, released on 18/6, plumes were measured, as detailed in the following. After a number of pre-release flights (no release was performed), for which, as expected, no plume could be detected, a series of overpasses were flown during the release of 15.12 kgCH_4/h between 11:10 and 12:00 local time on 18/6/2025. For 3 out of 20 overpasses, a spatially coherent enhancement could be observed, which fulfilled all criteria of plume detection: A spatially coherent enhancement, source coordinates close to the release point, lower average in-plume methane transmittance with respect to rest of the scene. The IME for all three detected plumes were <1 kgCH_4 compared to a mean IME of 2.93 kgCH_4 for the 79.2 kgCH_4/h releases on 17/6, providing further evidence that enhancements where of physical origin. Figure 10b shows the L3 result for the first detected plume, overpass 2367-2463 (11:13 local time, Table 2).

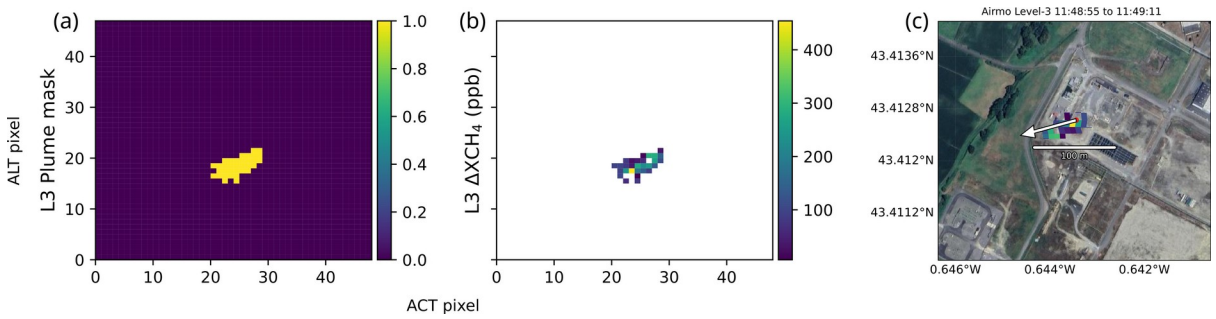

Figure 9. *L3 results for overpass 904-950 from 16/6/2025 in pixel space. ALT depicts along track, ACT across track. (a) Plume mask. (b) Plume enhancements. (c) Plume enhancements in coordinate space mapped onto aerial footage. Note that since no orthorectification was performed, pixels are distorted and non-uniform. A red dot marks the pixel with the maximum methane enhancement. The white arrow depicts the mean wind direction* θ_{mean} *from the MS of 80° (Table 2). Base photo data: Google tiles API.*

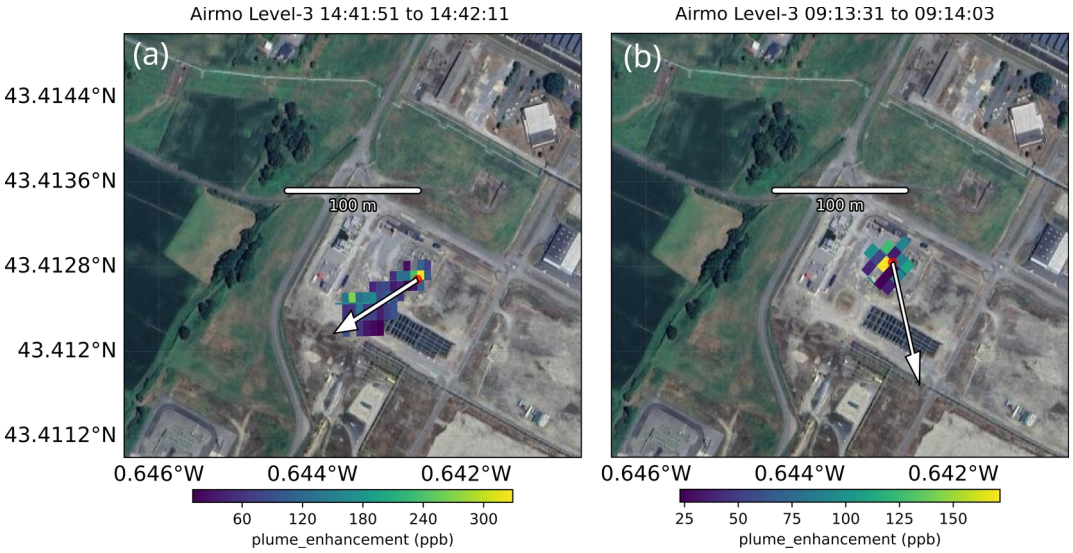

Figure 10. *L3 plume enhancements. (a) Overpass 3000-3060 from 17/6/2025, heading ~356°, i.e., north. (b) Overpass 2367-2463 from 18/6/2025, heading ~225°. The white arrow depicts the mean wind direction* θ_{mean} *from the MS (Table 2) Red dots marks retrieved source location. Times are UTC (local - 2 h). Base photo data: Google tiles API.*

Fluxes (L4 results) were computed employing (i) ERA5 and (ii) MS wind speeds. The retrieved flux for overpass 2367-2436 (Figure 10b) is 11 ± 10 kgCH_4/h using ERA5 wind speeds, and 30 ± 19 kg CH_4/h using the higher u_{eff} from MS wind (Table 2). Both values agree with the true release rate. Adopting the absolute minimum detectable enhancement of ~120 ppm.m, assuming u_{eff} ~1 m/s (Table 2) and a plume width of ~20 m, with Equation (9), this would correspond to a minimum detectable flux <15 kgCH_4/h. However, for this airborne geometry we do not deem 120 ppm.m a robust lower detection limit, but rather 500 ppm.m, as evaluated above, which would correspond to ~22 kgCH_4/h.

Although in agreement, the retrieved fluxes for 18/6 should be regarded with care. Wind speeds of ~0.7 m/s from ERA5 indicate nearly calm flow conditions during the overpasses on 18/6. MS wind speeds show substantial variability, ranging from ~0.5 m/s to ~2.7 m/s over the same period. Under these low and variable wind conditions, the detected methane enhancement is not collocated with the release point, but instead appears displaced by ~40 m upwind (Figure 10b). This spatial offset suggests that the assumption of steady and homogeneous plume transport underlying the flux retrieval may not be fulfilled in these cases.

The IME method (Equation (3)) assumes that plume transport can be approximated by a representative advection velocity u_{eff} and that the plume exhibits quasi-steady behaviour during the overpass. These assumptions are increasingly challenged under low wind speed conditions. For measured wind speeds below 1 m/s, plume transport is not necessarily dominated by mean wind advection, but also influenced by a combination of turbulent dispersion, density driven buoyancy, and

source momentum (Stull, 1988; Seinfeld and Pandis, 2016). As opposed to stronger winds, and in line with Equation (9), this facilitates higher pixel enhancements (Fisher, 2002) and thus easier plume detection. This has likely facilitated detecting plumes for 15.12 kgCH_4/h on 18/6 (Figure 10b). On the other hand, these conditions make flux quantification more uncertain, as the wind speed becomes a poor proxy for the effective plume transport velocity. This has several implications for the L4 retrieval. First, the plume may meander or remain spatially confined, such that the observed enhancement represents only a partial or transient plume structure rather than a steady plume. Second, as the plume length is retrieved from the detected plume pixel mask, the estimation of plume length becomes increasingly uncertain, contributing to over- or underestimated fluxes. Third, the semi-empirical relationship used here to derive effective plume speed is not well constrained in this regime, notably for u_{10} <0.6 m/s (Varon et al., 2018). Consequently, in these cases, u_{eff} was set to u_{10} since it was deemed the best estimate of u_{eff}. As both plume speed and plume geometry are subject to increased uncertainty under these conditions, the corresponding retrieved fluxes should be interpreted with caution. This includes overpasses 4088-4155, 5069-5133 and 5627-5693 (all 17/6, Table 2). For the underestimated flux for overpass 4088-4155, we furthermore note an abnormally low IME of 0.88 kgCH_4 compared to the mean of all overpasses for this emission rate of 2.93 kgCH_4.

The iterative scheme used to estimate u_{eff} yielded integration times between 30 s and 378 s. In one case it was 35 min and in 5 cases the iteration was stopped at 1 h maximum averaging time without convergence. Excluding these 6 cases, the mean averaging time over all overpasses in Table 2 was 117 s. As can be anticipated from the differences in wind speeds between ERA5 and MS at times (Figure 3), the averaging time window of u_{10} had a significant impact on L4 accuracy. To explore this dependency, for each release rate, the mean absolute error (MAE) of the retrieved fluxes with respect to the true release rate was evaluated. For the 104.4 kgCH_4/h release on 16/6, the MAE was comparable between MS and ERA5 wind speeds. For all other release rates, however, MAE for fluxes using MS u_{eff} were consistently higher than fluxes that used ERA5-derived u_{eff}. For example, for the 15 overpasses during the 79.2 kgCH_4/h release on 17/6 (Table 2), MAE was 22 kgCH_4/h (u_{eff} from ERA5) versus 30 kgCH_4/h (MS u_{eff} from iterative scheme).

The temporal averaging window for the MS u_{10} was then steadily increased manually. For all release rates, except for the aforementioned 104.4 kgCH_4/h release on 16/6, MAE reduced as a consequence, reaching a minimum MAE of 18 kgCH_4/h for the 79.2 kgCH_4/h releases on 17/6 at ~800 s (~13 min) averaging time, a reduction by ~12 kgCH_4/h compared to the initial MAE. As the averaging window approached 1 hour (ERA5 resolution), MAE increased again, eventually reaching 25 kgCH_4/h, which is similar to the MAE for ERA5. This suggests a strong dependence of IME-based flux accuracy to the temporal scale at which wind speed is defined. The shorter averaging windows, as yielded by the iterative method, may still be influenced by turbulent fluctuations, whereas longer

averaging windows (e.g. ERA5 hourly means), whilst approximating the effective transport timescale better than instantaneous or short-term in-situ measurements, may smooth out relevant variability. The optimal averaging window likely reflects an effective transport timescale over which turbulent fluctuations not representative of plume-scale advection are averaged out. In this case, this time frame lies between these two regimes. For the 104.4 kgCH_4/h release on 16/6, on the other hand, increasing the averaging time led to higher MAE, highlighting case-dependent behaviour.

This shows that the iterative method used here to arrive at the L4 values in Table 2 provides a physically consistent estimate of the effective transport velocity derived from local wind statistics, but it does not guarantee minimisation of flux error. It likely did not account for the temporal scales governing plume dispersion under the observed conditions. Given plume lengths of typically <200 m (Table 2), most integration times from the iterative method (<200 s) are consistent with expected plume residence times $t_{res} = l/u_{eff}$ (110 s average over all overpasses). As they do not yield the lowest flux errors, this suggests that plume transport cannot be fully described by a single advective timescale under the observed turbulent conditions. This discrepancy suggests that different timescales are being probed: the plume residence time describing the advective crossing time of the plume, and the optimal averaging time for flux retrieval reflecting the temporal scale over which turbulent fluctuations average out to yield a representative transport velocity u_{eff} for plume dispersion. This highlights a major limitation of the IME method.

Radiometric uncertainty (uncertainty in CH_4 enhancement) and plume speed uncertainty both dominate the error budget, with a mean relative radiometric uncertainty of 33% and a ERA5 wind speed uncertainty of 25% (averaged over all overpasses). The increase in wind speed variability with longer averaging windows reflects the inclusion of low-frequency fluctuations, which increases the estimated plume speed uncertainty (Equation (8)). For the MS derived fluxes, therefore, wind speed error dominates the error budget, with a mean relative uncertainty of 60%.

Figure 12 confronts retrieved fluxes with the true release rates. While Figure 12 does not suggest a distinct L4 bias and retrieved fluxes scatter fairly around the 1:1 line, there appears to be at least one outlier with an abnormally high retrieved flux of >300 kg for overpass 349-398 on 16/6. The overpass took place following a continuous release of methane at an elevated rate of 104.4 kg CH_4/h (≈2.4 m^3/min), implying that a substantial methane mass was present within the observed scene, supported by a unusually high IME of 8.6 kgCH_4. A friction velocity of 0.26 m/s suggests the presence of mechanically driven turbulence (Figure 3). However, this represents a single value at a spatial resolution of ~0.1° and may not be representative of local conditions. While turbulent transport likely influences plume dispersion, the spatial distribution of methane is governed by processes that are not resolved by the available observations, reflecting the combined influence of turbulent transport, local flow variability, and source characteristics. Therefore, the observed enhancement

cannot be unambiguously attributed to local accumulation (Fisher, 2002) and may instead reflect transient plume structures or variability in transport conditions.

For 17 out of the 19 overpasses total on 17/6/2025, flown within about 33 minutes, a methane plume could be detected and quantified (Table 2). The mean L4 result over the 17 overpasses is 64 ± 21 kgCH_4/h (76 ± 48 kgCH_4/h) with ERA5 (MS) wind speeds, in line with the true release rate of 79.2 kgCH_4/h. Although of limited robustness, given the small sample size, the standard deviations above provide an empirical measure of the effective L4 repeatability, taking into account all sources of uncertainty along the retrieval pipeline, such as, detector noise (L2) or false negative/positive pixels (L3) or plume speed error (L4).

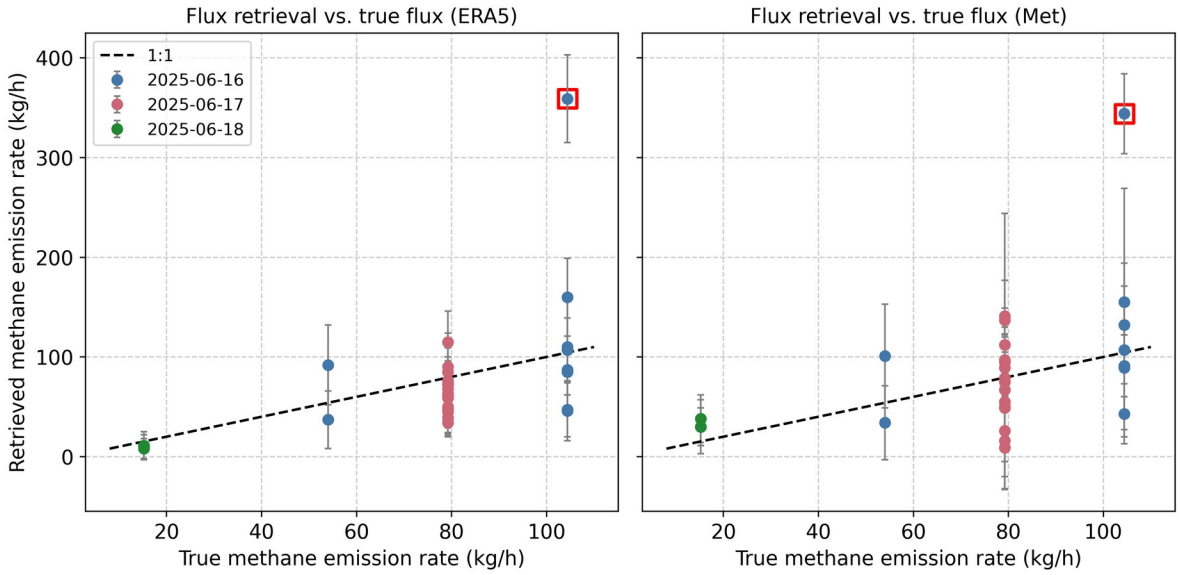

Figure 12. *L4 scatter plot. All valid retrieved L4 results (fluxes) with uncertainty bars (1 STD) against the true release rates for wind speeds from ERA5 and MS, color coded by day. Red boxes mark outlier (Overpass 349-398, Table 2).*

Summary and Conclusions

A SWIR push broom airborne demonstrator concept was evaluated during a single-blinded methane release experiment at the TADI test facility in Lacq (France), with release rates between 12.2 kgCH_4/h and 104.4 kgCH_4/h. The objective was to assess the system's capability to detect methane plume enhancements and derive indicative emission estimates under realistic atmospheric conditions.

From the 67 measurement flights, 4 were pre-release flights. For 3 overpasses, on 16/6/2025, opaque cloud cover beneath the aircraft prevented measurements. From the remaining 60 flights, for 30 overpasses, listed in Table 2, a plume could be detected and the corresponding CH_4 flux quantified

(50% rate of detection). For 24 overpasses, release rates were 15.2 kgCH_4/h or less. From these, in 3 cases a plume was detected and quantified, leaving 36 overpasses during clear sky with release rates ≥54 kgCH_4/h, with an associated detection rate of 27/36 or ~75%.

Uncertainties for the 30 overpasses in Table 2 ranged between 12% and 229%, dominated by radiometric noise and wind-speed uncertainty. The corresponding mean uncertainty is 59% (average of mean ERA5 and mean MS uncertainty), which is compatible to similar tests (Frankenberg et al., 2016; Chulakadabba et al., 2023).

This campaign represents a first proof of concept for the AIRMO payload and its data-processing pipeline and a promising step toward an improved instrument design with reduced systematic and random errors. Work is ongoing to reduce instrument-induced errors, in particular to correct the likely smile-related artifacts at the hardware level and contributions from spatial stray light. This is expected to increase the usable swath and improve both precision (thus sensitivity) and bias. The objective is to achieve sensitivities that enable robust quantification of methane fluxes well below 20 kg/h for airborne measurements.

The L4 accuracy was found to be sensitive to the temporal averaging window used to obtain effective wind speed (plume speed). The results of this study indicate that ERA5 reanalysis winds may yield lower flux errors in some cases, likely because their temporal and spatial averaging better approximates the effective plume-scale advection velocity. High-frequency in-situ wind measurements can in principle provide more accurate flux estimates, provided that an appropriate averaging timescale is chosen to represent plume-scale transport dynamics. However, determining this timescale from wind data alone proved challenging, highlighting a fundamental limitation of IME-based flux retrievals, particularly under low and highly variable wind conditions.

Acknowledgments

The authors would like to thank Jochen Landgraf and Herbert Nett for their ongoing support and valuable input. Furthermore, our gratitude goes to TADI for the testing and validation opportunity. The project received funding from the ESA InCubed programme (ESA Contract No. 4000141570/23/I-DTO) and from the Luxembourg Space Agency (ESA Contract No. 4000144851/24/NL/VR). We thank Kamal Sharma for helpful comments and for proofreading the manuscript.

Disclosure statement

No potential conflict of interest was reported by the author(s).

Data availability

All data (raw data up to L4) that support the findings and scripts to process the high level data for this study are available on individual request from the corresponding authors, MQ, KV, and DV.

References

Beirle, S., J. Lampel, C. Lerot, H. Sihler, and T. Wagner. 2017. “Parameterizing the instrumental spectral response function and its changes by a super-Gaussian and its derivatives.” *Atmospheric Measurement Techniques* 10: 581–598. doi:10.5194/amt-10-581-2017.

Bruno, J. H., D. Jervis, D. J. Varon, and D. J. Jacob. 2024. “U-Plume: Automated algorithm for plume detection and source quantification by satellite point-source imagers.” *Atmospheric Measurement Techniques* 17: 2625–2636. doi:10.5194/amt-17-2625-2024.

Bukosa, B., S. Mikaloff-Fletcher, A. Geddes, D. Pollard, S. Moore, R. Law, D. Noone, M. Sargent, J. Benmergui, and S. Wofsy. 2024. “How well can MethaneSAT detect and quantify pastoral agricultural emissions?” *EGU General Assembly 2024*, Vienna, Austria. doi:10.5194/egusphere-egu24-4484.

Burrows, J. P., M. Weber, M. Buchwitz, V. Rozanov, A. Ladstätter-Weißenmayer, A. Richter, R. De Beek, R. Hoogen, K. Bramstedt, K.-U. Eichmann, M. Eisinger, and D. Perner. 1999. “The Global Ozone Monitoring Experiment (GOME): Mission concept and first scientific results.” *Journal of the Atmospheric Sciences* 56: 151–175.

Burton, M. R., G. M. Sawyer, and D. Granieri. 2013. “Deep carbon emissions from volcanoes.” In *Deep Carbon: Past to Present*, edited by B. N. Orcutt, I. Daniel, and R. Dasgupta, 323–354. Cambridge: Cambridge University Press. doi:10.2138/rmg.2013.75.11.

Butz, A., A. Galli, O. Hasekamp, J. Landgraf, P. J. J. Tol, and I. Aben. 2012. “TROPOMI aboard Sentinel-5 Precursor: Prospective performance of CH_4 retrievals for aerosol and cirrus loaded atmospheres.” *Remote Sensing of Environment* 120: 267–276. doi:10.1016/j.rse.2011.05.030.

Callies, J., E. Corpaccioli, M. Eisinger, A. Hahne, and A. Lefebvre. 2000. “GOME-2–Metop’s second-generation sensor for operational ozone monitoring.” *ESA Bulletin* 102: 28–36.

Chan Miller, C., S. Roche, J. S. Wilzewski, X. Liu, K. Chance, A. H. Souri, E. Conway, B. Luo, J. Samra, J. Hawthorne, K. Sun, C. Staebell, et al. 2024. “Methane retrieval from MethaneAIR using the CO_2 proxy approach.” *Atmospheric Measurement Techniques* 17: 5429–5454. doi:10.5194/amt-17-5429-2024.

Chulakadabba, A., M. Sargent, T. Lauvaux, J. S. Benmergui, J. E. Franklin, C. Chan Miller, J. S. Wilzewski, S. Roche, E. Conway, A. H. Souri, K. Sun, B. Luo, et al. 2023. “Methane point source quantification using MethaneAIR.” *Atmospheric Measurement Techniques* 16: 5771–5785. doi:10.5194/amt-16-5771-2023.

Coddington, O. M., E. C. Richard, D. Harber, P. Pilewskie, T. N. Woods, K. Chance, et al. 2021. “The TSIS-1 hybrid solar reference spectrum.” *Geophysical Research Letters* 48: e2020GL091709. doi:10.1029/2020GL091709.

Crisp, D., H. R. Pollock, R. Rosenberg, L. Chapsky, R. A. M. Lee, F. A. Oyafuso, C. Frankenberg, C. W. O’Dell, C. J. Bruegge, G. B. Doran, A. Eldering, B. M. Fisher, et al. 2017. “The on-orbit performance of OCO-2.” *Atmospheric Measurement Techniques* 10: 59–81. doi:10.5194/amt-10-59-2017.

Cusworth, D. H., A. K. Thorpe, C. E. Miller, A. K. Ayasse, R. Jiorle, R. M. Duren, R. Nassar, J.-P. Mastrogiacomo, and R. R. Nelson. 2023. “Two years of satellite-based CO_2 emission quantification.” *Atmospheric Chemistry and Physics* 23: 14577–14591. doi:10.5194/acp-23-14577-2023.

Dandenault, P. B., E. Dao, S. R. Kaeppler, and E. S. Miller. 2020. “Estimation of human-error contributions to historical ionospheric data.” *Earth and Space Science* 7: e2020EA001123. doi:10.1029/2020EA001123.

Duren, R., D. Cusworth, A. Ayasse, K. Howell, A. Diamond, T. Scarpelli, J. Kim, K. O’Neill, J. Lai-Norling, A. Thorpe, S. R. Zandbergen, L. Shaw, et al. 2025. “The Carbon Mapper emissions monitoring system.” *EGUsphere* preprint. doi:10.5194/egusphere-2025-2275.

Fisher, B. 2002. “Meteorological factors influencing the occurrence of air pollution episodes involving chimney plumes.” *Meteorological Applications* 9: 199–210. doi:10.1017/S1350482702002050.

Frankenberg, C., J. F. Meirink, M. van Weele, U. Platt, and T. Wagner. 2005. “Assessing methane emissions from global space-borne observations.” *Science* 308: 1010–1014.

Frankenberg, C., U. Platt, and T. Wagner. 2005. “IMAP-DOAS for strongly absorbing trace gases.” *Atmospheric Chemistry and Physics* 5: 9–22. doi:10.5194/acp-5-9-2005.

Frankenberg, C., A. K. Thorpe, D. R. Thompson, G. Hulley, E. A. Kort, N. Vance, J. Borchardt, T. Krings, K. Gerilowski, C. Sweeney, S. Conley, B. D. Bue, et al. 2016. “Airborne methane remote measurements in the Four Corners region.” *Proceedings of the National Academy of Sciences of the USA* 113 (35): 9734–9739. doi:10.1073/pnas.1605617113.

Gerilowski, K., A. Tretner, T. Krings, M. Buchwitz, P. P. Bertagnolio, F. Belemezov, J. Erzinger, J. P. Burrows, and H. Bovensmann. 2011. “MAMAP spectrometer system.” *Atmospheric Measurement*

Techniques 4: 215–243. doi:10.5194/amt-4-215-2011.

Giusti, M., ed. 2022. *Copernicus Arctic Regional Reanalysis (CARRA): Data User Guide*. ECMWF.

Gordon, I. E., L. S. Rothman, R. J. Hargreaves, R. Hashemi, E. V. Karlovets, F. M. Skinner, et al. 2022. "The HITRAN2020 database." *Journal of Quantitative Spectroscopy and Radiative Transfer* 277: 107949. doi:10.1016/j.jqsrt.2021.107949.

Guanter, L., H. Kaufmann, K. Segl, S. Foerster, C. Rogass, S. Chabrillat, T. Kuester, A. Hollstein, G. Rossner, C. Chlebek, C. Straif, et al. 2015. "The EnMAP mission." *Remote Sensing* 7: 8830–8857. doi:10.3390/rs70708830.

IPCC. 2021. "Summary for policymakers." In *Climate Change 2021: The Physical Science Basis*, edited by V. Masson-Delmotte et al. Cambridge: Cambridge University Press.

Jacob, D. J., D. J. Varon, D. H. Cusworth, P. E. Dennison, C. Frankenberg, R. Gautam, L. Guanter, J. Kelley, J. McKeever, L. E. Ott, B. Poulter, Z. Qu, et al. 2022. "Quantifying methane emissions globally to point sources." *Atmospheric Chemistry and Physics* 22: 9617–9646. doi:10.5194/acp-22-9617-2022.

Kleipool, Q., A. Ludewig, L. Babić, R. Bartstra, R. Braak, W. Dierssen, P.-J. Dewitte, P. Kenter, R. Landzaat, J. Leloux, E. Loots, et al. 2018. "Pre-launch calibration of TROPOMI." *Atmospheric Measurement Techniques* 11: 6439–6479. doi:10.5194/amt-11-6439-2018.

Kondo, M., K. Ichii, H. Takagi, and M. Sasakawa. 2015. "Comparison of the data-driven top-down and bottom-up global terrestrial CO_2 exchanges." *Journal of Geophysical Research: Biogeosciences* 120: 1226–1245. doi:10.1002/2014JG002866.

Krings, T., B. Neininger, K. Gerilowski, S. Krautwurst, M. Buchwitz, J. P. Burrows, C. Lindemann, T. Ruhtz, D. Schüttemeyer, and H. Bovensmann. 2018. "Airborne CO_2 quantification." *Atmospheric Measurement Techniques* 11: 721–739. doi:10.5194/amt-11-721-2018.

Landgraf, J., A. Butz, O. Hasekamp, H. Hu, and J. aan de Brugh. 2019. *Sentinel-5 L2 Prototype Processors: Methane Retrieval ATBD*. SRON.

Li, X., Y. Zhang, G. de Leeuw, X. Yao, Z. He, H. Wu, and Z. Yang. 2025. "A review of city-scale methane flux inversion based on top-down methods." *Remote Sensing* 17: 3152. doi:10.3390/rs17183152.

MacLean, J.-P. W., M. Girard, D. Jervis, D. Marshall, J. McKeever, A. Ramier, M. Strupler, E. Tarrant, and D. Young. 2024. "Offshore methane detection with GHGSat." *Atmospheric Measurement Techniques* 17: 863–874. doi:10.5194/amt-17-863-2024.

Mazzini, A., A. Sciarra, and G. Etiope. 2021. “Relevant methane emission to the atmosphere from a geological gas manifestation.” *Scientific Reports* 11: 4138. doi:10.1038/s41598-021-83369-9.

Mouroulis, P., R. O. Green, and T. G. Chrien. 2000. “Design of push broom imaging spectrometers for optimum recovery of spectroscopic and spatial information.” *Applied Optics* 39 (13): 2210–2220. doi:10.1364/AO.39.002210.

Nisbet, E. G., E. J. Dlugokencky, and P. Bousquet. 2014. “Methane on the rise—again.” *Science* 343: 493–495. doi:10.1126/science.1247828.

Noël, S., M. Buchwitz, and J. P. Burrows. 2004. “First retrieval of global water vapour from SCIAMACHY.” *Atmospheric Chemistry and Physics* 4: 111–125. doi:10.5194/acp-4-111-2004.

Paškevičiūtė-Kidron, A. 2025. “Overview of risk retirement for ESA’s TANGO mission.” In *Proceedings of SPIE: Small Satellites Systems and Services Symposium (4S 2024)*, Vol. 13546. doi:10.1117/12.3061921.

Rodgers, C. D. 2000. *Inverse Methods for Atmospheric Sounding: Theory and Practice*. Singapore: World Scientific.

Roger, J., L. Guanter, and J. Gorroño. 2025. “Detection of methane plumes in offshore areas.” *EGUsphere* preprint. doi:10.5194/egusphere-2025-1917.

Schönhardt, A., P. Altube, K. Gerilowski, S. Krautwurst, J. Hartmann, A. C. Meier, A. Richter, and J. P. Burrows. 2015. “Wide FOV imaging DOAS instrument.” *Atmospheric Measurement Techniques* 8: 5113–5131. doi:10.5194/amt-8-5113-2015.

Seinfeld, J. H., & Pandis, S. N., 2016. “Atmospheric Chemistry and Physics: From Air Pollution to Climate Change” (3rd ed.). Wiley, ISBN ISBN: 978-1-118-94740-1.

Sherwin, E. D., J. S. Rutherford, Y. Chen, et al. 2023. “Validation of space-based methane point-source detection.” *Scientific Reports* 13: 3836. doi:10.1038/s41598-023-30761-2.

Stull, R. B. 1988. “An Introduction to Boundary Layer Meteorology”. Springer, ISBN 9027727694.

Thompson, D. R., I. Leifer, H. Bovensmann, M. Eastwood, M. Fladeland, C. Frankenberg, K. Gerilowski, R. O. Green, S. Krautwurst, T. Krings, B. Luna, and A. K. Thorpe. 2015. “Real-time remote detection using airborne spectroscopy.” *Atmospheric Measurement Techniques* 8: 4383–4397. doi:10.5194/amt-8-4383-2015.

Thorpe, A. K., R. O. Green, D. R. Thompson, P. G. Brodrick, J. W. Chapman, C. D. Elder, I. Irakulis-Loitxate, D. H. Cusworth, A. K. Ayasse, R. M. Duren, C. Frankenberg, et al. 2023. “Attribution of methane and CO_2 using EMIT.” *Science Advances* 9: eadh2391. doi:10.1126/sciadv.adh2391.

Varon, D. J., D. J. Jacob, J. McKeever, D. Jervis, B. O. A. Durak, Y. Xia, and Y. Huang. 2018.

765 “Quantifying methane point sources from satellite observations.” *Atmospheric Measurement Techniques* 11: 5673–5686. doi:10.5194/amt-11-5673-2018.

Veefkind, J. P., I. Aben, K. McMullan, H. Förster, J. de Vries, G. Otter, J. Claas, H. J. Eskes, J. F. de Haan, Q. Kleipool, M. van Weele, et al. 2012. “TROPOMI on Sentinel-5P.” *Remote Sensing of Environment* 120: 70–83. doi:10.1016/j.rse.2011.09.02.

770 Wolff, S., G. Ehret, C. Kiemle, A. Amediek, M. Quatrevalet, M. Wirth, and A. Fix. 2021. “Determination of the emission rates of CO_2 point sources with airborne lidar.” *Atmospheric Measurement Techniques* 14: 2717–2736. doi:10.5194/amt-14-2717-2021.

775

Supplementary Material for

Airborne measurements of methane releases under turbulent wind with an imaging spectrometer

Manuel Queißer[1*], Kirill Volter[1], Mohd Bilal[1], Igor Mishin[1], Luke Fries[1], David Vilaseca[1], Zhuldyz Darynova[2], Catherine Juery[3], Errico Armandillo[1], Ravil Idrisov[1], Daria Stepanova[1]

[1]AIRMO GmbH, Berlin, Germany

[2]SeaOwl Energy Services, Toronto, Canada

[3]TotalEnergies, R&D, DEMETER Remote Sensing Team, Pau, France

Supplementary Methods

S1 Calibration key data

After the PB was optically aligned and focused, a set of calibration key data (CKD) was acquired during preflight characterization. The CKD are needed to process the raw spectra (L0) to L1B spectra and are unique to the PB system and may be re-acquired in intervals.

For dark noise retrieval, the detection chain offset (DCO) and dark noise are measured as a function of integration time (Figure S1). Following Paškevičiūtė-Kidron et al. (2024), a default detector temperature of 15°C is used per default for all acquisitions. From these data, a reference dark noise frame is retrieved and saved to the CKD. This is used to scale dark noise to the integration time of the science frames, usually a couple of hundred ms. The dark frames are furthermore used to derive a hot pixel map, a mask of consistently abnormally high pixel values, indicating positions of pixels that have unusually high dark currents, e.g. due to crystal defects or cosmic radiation damage, in case of space borne deployment.

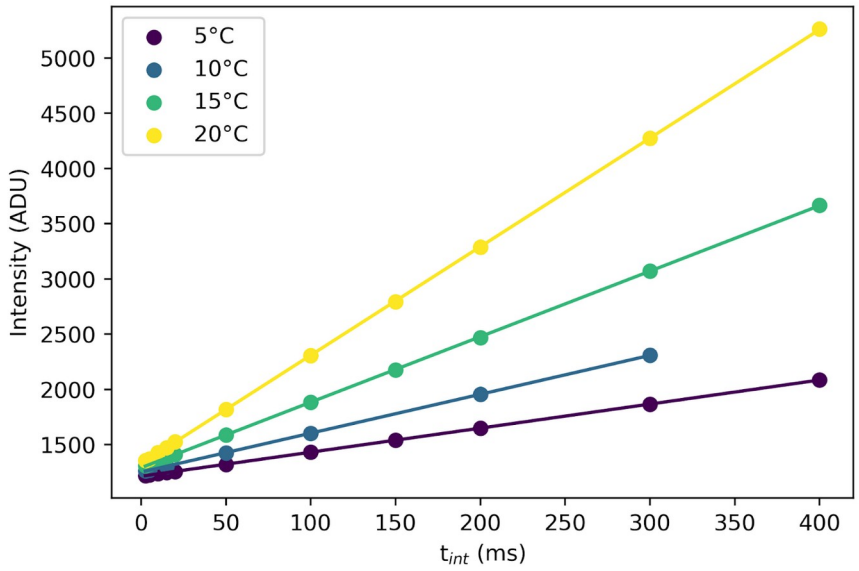

Figure S1. *Mean dark noise over frame as a function of integration time and for different detector temperatures. The dark current offset is the y-axis.*

For spectral calibration, a Fabry Perot Etalon (FPE, Light-Machinery OP5973), illuminated by a white light source (WLS), mounted on an angle cradle, is used to generate interference fringes for a number of different across track angles (Figure S2a). The across track dimension is divided into 5 sectors each corresponding to a given angle. A Gaussian fit yields inter-pixel peak positions. Knowing the free spectral range (FSR) frequency of the FPE, the FSR in wavelength domain is

calculated (~1.8 nm depending on spectral wavelength) and, using an absolute wavelength calibration from a 1550 nm narrow linewidth laser, the pixel/wavelength calibration grid is generated.

The Fabry Perot (FP) frames are also used to obtain the instrumental response function (ISRF) of the PB as a function of the 5 across track angle sectors and wavelength. Since the FP transmission peaks are only ~20 pm wide, it is a fair assumption that the instrument's spectral resolution is significantly broader than the FP transmission peaks (Figure S2b). Super Gaussian functions (Beirle et al., 2017), and Gaussians for reference, are directly fitted to the dark noise corrected FP interference maxima. Figure S2b shows an example fit, including the width w, which is half of the full width at 1/e maximum (FWEM), and the asymmetry parameter k. For k = 2 the function approaches a normal Gaussian, and for k just over 2, as retrieved here, it models a flat top curve. Fitting parameters as a function of central wavelengths are saved to the CKD.

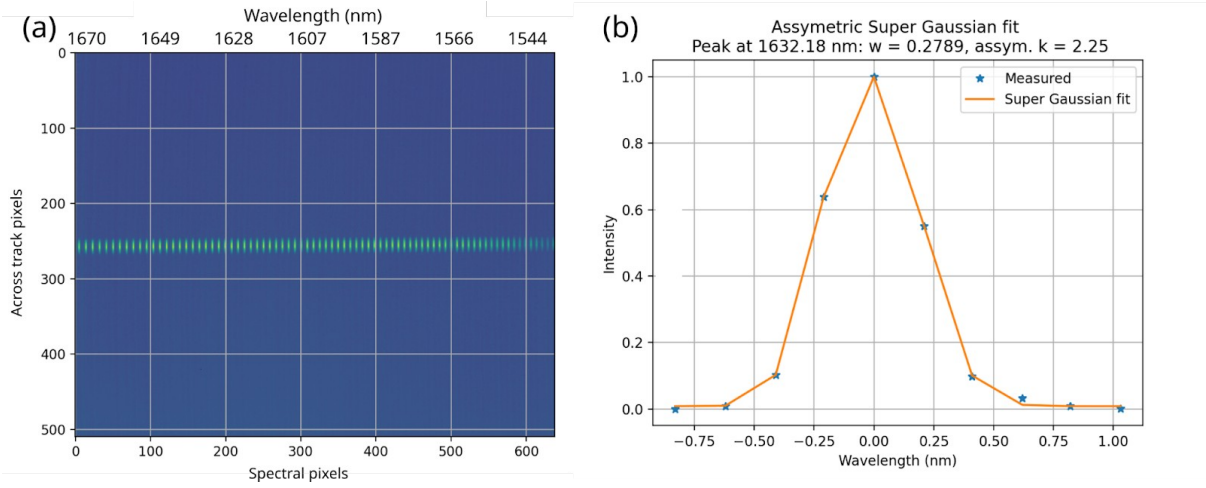

Figure S2. *Spectral calibration with a Fabry Perot (FP) interferometer. (a) Frame with FP fringes at 0° across track angle. (b) Example Super Gaussian fit of a FP peak with width and asymmetry parameter at central wavelength 1632.18 nm.*

The quantum efficiencies (QE) of the pixels differ across the array, for instance, due to the manufacturing process (Kleipool et al., 2018). This Pixel Response Non-Uniformity (PRNU) may cause biased trace gas retrieval. To characterise the PRNU, a dedicated setup consisting of WLS and a diffuser arrangement is used. A sufficiently high number of frames needed to produce an average flat field response is acquired. After dark noise correction, the PRNU correction frame is retrieved by dividing the mean flat field response frame by a smoothed version along the spectral dimension. Initially, only the detector array was illuminated, excluding the objective optics. Since the latter may also give rise to relative response variations on a small scale (on a pixel-by-pixel level), at a later stage the complete spectrometer optical train is included in the characterization. Thus, the flat field response includes all wavelength dependent PRNU effects, including QE, grating efficiency, and lens/mirror losses. In addition to spectral PRNU correction, correcting for PRNU across track is done.

The procedure is equivalent to the spectral PRNU correction, except that smoothing occurred along the across track dimension.

A setup similar to the one used for ISRF characterization is used to characterise the optical transmission as a function of wavelength of the optical chain of the spectrometer. Using the WLS and the angle cradle, frames are acquired for the five different angular sectors. The measured WLS spectra can be written as $I_0(\lambda)=S_{WLS}(\lambda)T(\lambda)$, where λ is the wavelength, $S_{WLS}(\lambda)$ is the spectrum of the WLS and $T(\lambda)$ is the desired spectral transmission. The latter is retrieved by dividing dark noise, PRNU and hot pixel corrected WLS spectrum $I_0(\lambda)$ by the theoretical spectrum of the WLS $S_{WLS}(\lambda)$.

To correct smile, an optical distortion caused by the slit illumination (Mouroulis et al., 2000), the smile is measured by illuminating the detector wit the Fabry Perot interferometer at different angles of incidence, and fitting circles to the resulting curved columns. From these, a shift matrix that contains the amount of shift in pixels for each detector pixel is constructed.

S2 Data processing

Starting from the SRON open source Toolbox for End-to-enD Simulations (TEDS, https://teds.readthedocs.io/en/latest, last accessed 26/10/2025), a real data processing pipeline from raw data to Level-4 has been developed and is continuously being improved. The code, in the following referred to as End-to-End (E2E), serves as both an end-to-end simulator and a real data processing pipeline for both satellite and airborne viewing geometry.

S2.1 Level 1B processing

Science data are pre-processed from the raw spectra (L0 data) into geolocated, instrument corrected spectra (Level 1B, L1B), as detailed in the following. For each overpass over the release site, science spectrometer frames within the area of interest (tens of frames) were merged into data cubes with dimension along-track, across track and spectral pixels. Position velocity and time (PVT) data are extracted from the IMU and used to generate a geometry data NetCDF file for each data cube. The data of this file are used to accurately georeference each pixel of the data cube and to retrieve viewing angles and solar angles, including solar zenith angles (SZA), needed for L2 processing. No orthorectification, such as regridding or gap filling, is applied. However, using the geometry data file, geo-referencing and instrument-to-ground distances are corrected for aircraft pitch, yaw and roll.

Dark noise correction is performed, using detector DCO (Figure S1) and reference dark frame (at reference exposure time) from CKD (Figure S3). This is followed by interpolating hot pixels, which otherwise would create positive or negative spikes. It is assumed here that dark noise, and thus, hot pixel characterization remains unchained for extended periods of time. This has been verified by repeating the DCO and dark noise characterization over weeks and months. After two months, DCO

drifted by ~0.2% only. For space applications this situation would certainly change, for instance, to the interference of the detector array with cosmic rays which would make hot pixel characterization a more frequent task.

Next, despiking is applied, which involves comparing the difference of each spectral pixel value and a smoothed version of it (from Savgol filtering) with a carefully adjusted threshold.

This is followed by PRNU correction, where the spectra for each act-pixel are divided by the flat field response from CKD. Subsequently, across track PRNU correction is applied. After that, instrument spectral transmission correction and wavelength calibration using the wavelength grid from CKD are carried out, followed by wavelength fine-adjustment to correct for coarse shifts in wavelength between each across track row of the science frame and simulated TOA spectra using cross correlation.

A spectral smile, an optical distortion effect, is apparent for all frames. An example is given in Figure S3. Smile is corrected by applying the desmiling matrix from the CKD. It shifts each pixel for each across track row to its supposed spectral position.

Next, pixel binning is carried out, which means, across track averaging of pixel photon counts at the software level. No co-adding of frames (grouping) is applied. Several binning factors between 2 and 15 were tested. As expected from theory, the signal-to-noise-ratio (SNR) did not improve significantly beyond a binning factor of about 10, whilst spatial resolution keeps degrading linearly with binning factor increase. A binning factor of 10 was consequently settled upon and used for all acquisitions. This results in a ground sampling distance of ~9 m in the across track dimension.

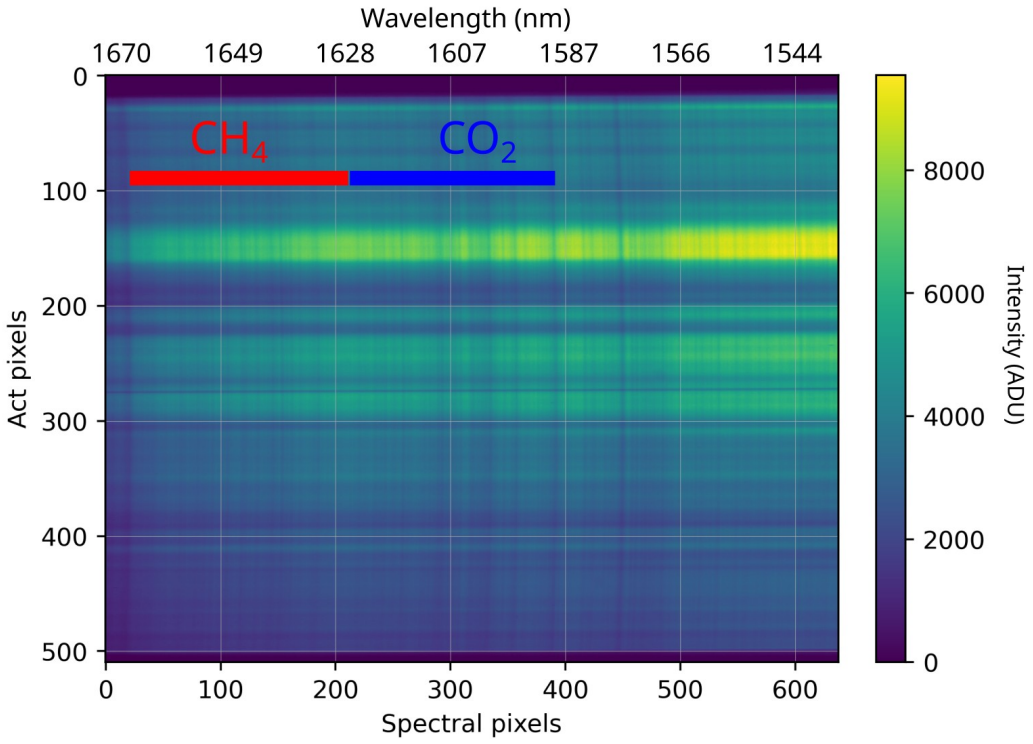

Figure S3. *Example dark noise corrected science frame during L1B processing showing across track (act) pixels and spectral pixels (wavelength is reversed) before PRNU correction. Curved absorption features, e.g., at spectral pixel 445 (CO_2) and the dark line around pixel 20 (CH_4 absorption band around 1666 nm) indicate a smile effect.*

S2.2 Level-2 processing

Each L1b spectra of a given data cube, is processed by minimizing the mismatch between a forward modeled spectrum using a nonscattering radiative transfer model and the measured spectrum, resulting in XCH_4 images (Level-2 products, L2). The fit range used is 1594 nm to 1660 nm. The CH_4 absorption band around 1666 nm (Figure S3), which is strongly absorbing, is excluded to minimise nonlinearity between line depth and measured light intensity.

The atmospheric module of the E2E creates vertical profiles of atmospheric dry air pressure, temperature, and layer-integrated partial column densities VCD_j (in cm^{-2}) for layer j of the following species: dry air and the trace gases CH_4, CO_2 and H_2O. Example profiles are shown in Figure S4. To that end, ERA5 complete data from the European Centre for Medium-Range Weather Forecasts (ECMWF) closest to the mid-scene coordinates is used, providing pressure, temperature, relative and specific humidity for selected pressure levels and isobaric altitudes. From the humidity profiles, $VCD_{H2O,j}$, XH_2O and vapour pressure are retrieved. The latter is used to obtain the dry air column density $VCD_{air,j}$. To create $VCD_{CO2,j}$ and $VCD_{CH4,j}$, XCO_2 is taken from the US standard atmosphere, whilst a vertically constant XCH_4 is assumed.

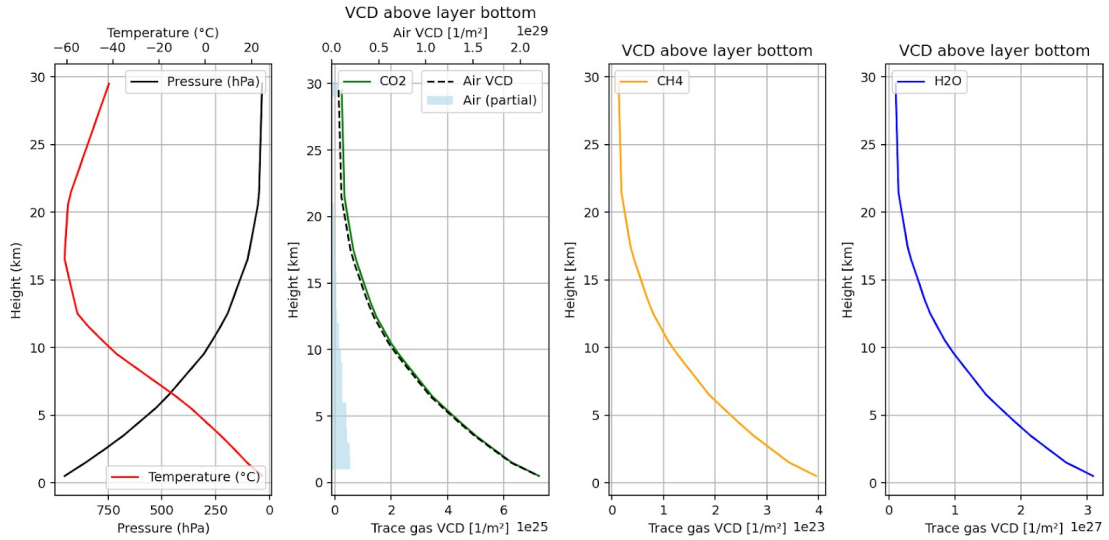

Figure S4. *Modeled atmosphere from reanalysis data for Lacq (France) from 16/6/2025 12:00 UTC (14:00 local time). The data are plotted against 30 model layers, which is the midpoint between layers. The light blue histogram shows the per layer dry air partial column density.*

Synthetic spectra are computed using the following non-scattering radiative transfer forward model:

$$y_{fwd}(\lambda) = ISRF(\lambda') \otimes \left(I_{sun}(\lambda) \sum_{l}^{L} P_l(\lambda) \frac{\cos(SZA)}{\pi} \exp\left[-\sum_{j}^{nlay} \tau_j(\lambda) u \right] \right), \quad \text{(S1)}$$

where $u = \frac{1}{\cos(SZA)} + \frac{1}{\cos(VZA)}$ is the air mass factor, with the solar zenith and viewing zenith angles SZA and VZA, respectively. ISRF is the instrumental spectral response function of the spectrometer. $\tau_j(\lambda)$ are the total gas optical depths per z-layer j (unitless). These are computed as the sum of the optical depths of all three trace gas species modeled (CO_2, CH_4, H_2O), which in turn are the product of the absorption cross section and the vertical column densities per vertical layer, written as (Landgraf et al., 2019)

$$\tau_j(\lambda) = \sum_{i}^{gas} \sigma_{ij}(\lambda) VCD_{ij}(z) \quad \text{(S2)}$$

where $\sigma_{ij}(\lambda)$ is the absorption cross section of molecule i at vertical layer j, calculated using spectroscopic parameters from the HITRAN database (Gordon et al., 2020). $I_{sun}(\lambda)$ is a high resolution literature Fraunhofer spectrum retrieved from space observation (Coddington et al., 2021). Background polynomials are commonly used to model broadband scattering (e.g., Frankenberg et al., 2005a; Schönhardt et al., 2015). Here, $P_l(\lambda)$ is a Legendre background polynomial of degree L=5, which accounts for surface reflectance (Cusworth et al., 2019).

Note that the science spectra currently do not undergo radiometric calibration. Instead, they have been linearly scaled to match the mean intensity of the simulated spectra with similar observation geometry. During end-to-end simulations it was found that this leads to an insignificant bias in the retrieved trace gas column density as the first Legendre coefficient absorbs changes in the intensity of the forward modeled spectra during the optimization in the L2 fitting. That also means that the final L2 images of albedo and Legendre coefficient represent relative distribution map of surface reflectivity rather than absolute surface reflectivity

The forward modeled spectra y_{fwd}, are nonlinear in x and thus linearised around x_0 as a Taylor expansion of first order (Frankenberg et al., 2005a; Butz et al., 2012):

$$y_{meas}(x) \approx y_{fwd}(x_0) + K(x - x_0) + error. \quad \text{(S3)}$$

x depicts the state vector ,

$$x = (s_{CH_4}, s_{CO_2}, s_{H_2O}, p0, p1, p2, p3, p4, \Delta\lambda, S),$$

which contains all model arguments that are being optimised in the forward modeling process during the fitting, where s_{CH_4}, s_{CO_2}, s_{H_2O} are the profile scaling factors for CH_4, CO_2 and H_2O, respectively, followed by the first 5 Legendre polynomial coefficients and the spectral shift $\Delta\lambda$ and stretch parameter S, which compensate imperfect wavelength calibration and drifts of the latter over time. x_0 represents the initial guess state vector. K is the Jacobian matrix, i.e., the derivative of the forward modeled spectra (for each wavelength bin m) with respect to the nth state vector parameters. The components of K can be written as

$$K_{mn} = \frac{\partial y_{fwd,m}}{\partial x_n}. \quad \text{(S4)}$$

Equation (3) is solved iteratively by optimizing the least square difference between measured and modeled spectra for each pixel as

$x = argmin(||y_{fwd} - y_{meas}||)$ until convergence is achieved with the iterative solution

$$x_{k+1} = x_k + G(y_{fwd} - y_{meas}) \quad \text{(S5)}$$

where G is the gain matrix, computed using a Levenberg Marquardt scheme,

$$G = \left(S_x K^T S_y^{-1} + \Lambda I\right)^{-1}, \quad \text{(S6)}$$

where S_y^{-1} is inverse of the measurement covariance matrix, I is the unity matrix and Λ is a damping factor, S_x is the covariance matrix of the least square solution, $S_x = \left(K^T S_y^{-1} K\right)^{-1}$.

For each of the three trace gases, the atmosphere module calculates an initial guess (reference) profile of layer integrated partial column densities (VCD in molec.m^{-2}), $VCD_{i,j}(z)$, one per each of the $nlay$ layers, scaled to an initial guess mixing ratio. At each iteration k, the reference profiles of each gas i (CH_4, CO_2, H_2O) is scaled by the column scaling factor for each gas as

$$VCD_{i,j,k+1}(z) = s_i \, VCD_{i,j,k}(z). \quad \text{(S7)}$$

Once Equation (S3) converges, the dry air volume mixing ratios (VMR), XCH_4, XCO_2, XH_2O are computed from the final $VCD_{i,j}(z)$ as

$$VMR_i = \frac{\sum_j^{nlays} VCD_{i,j}}{\sum_j^{nlays} VCD_{air,j}} \quad \text{(S8)}$$

To correct for aerosol scattering, including multiple scattering (e.g., between surface and

aerosols) the proven CO_2-proxy method is applied (Frankenberg et al., 2005b; Krings et al., 2011; Chan Miller et al., 2024) so that the effect of scattering cancels out by scaling the methane *VCD* with the CO_2 *VMR* to *VCD* ratio, i.e.,

$$VMR_{CH_4} = \frac{VCD_{CH_4}}{VCD_{CO_2}} VMR_{CO_2,av}\,, \tag{S9}$$

where $VMR_{CO_2,av}$ is the climatological mean of the CO_2 mixing ratio over the sounding area.

S3.3 Level-3 processing

Plume detection, i.e., the decision of whether the XCH_4 image contains a plume or not, is essentially separating two populations: the background XCH_4 and the plume XCH_4 (e.g., Cusworth et al., 2023; Roger et al., 2025). A relatively straightforward image processing based algorithm is used to delineate plumes by detecting statistically significant enhancements in XCH_4. The detection algorithm consists of denoising the spatial XCH_4 map, followed by a well-known z-test, which identifies pixels that are likely enhanced in CH_4 concentration compared to a local background measure, for which the median XCH_4 map is calculated. It is based on the pixel's value, the local variance and the threshold confidence parameter q. In the second step, clustering is performed. Only clusters of pixels that have a minimum number N_{min} of pixels passing the z-test are kept to further reduce noise. A plume is detected when at least one cluster has been identified. This separation is termed segmentation. The defining parameters of the detection algorithm are therefore q and N_{min}. Their behavior and optimal values have been studied statistically when defining mission requirements for AIRMO-Space. It has been found that more sophisticated machine learning approaches can achieve similar false positive/negative rates performance at significantly worse L2 precision, which suggests our requirements for q and N_{min} are conservative. Where needed, pixels contaminated by clouds can be filled-in through interpolation or plume models. For this campaign, however, only cloud free data are considered. At this stage, a simple source localization is performed, as the coordinate of the pixel with the highest CH_4 enhancement.

S2.4 Level-4 processing

The isolated and attributed plume is used, together with wind estimates, to retrieved the methane mass emission rate (flux) using the integrated mass enhancement (IME) method (Frankenberg et al., 2016; Varon et al., 2018):

$$\phi = \frac{u_{eff}}{l} IME \tag{S10}$$

where ϕ is the CH_4 flux (in kg/s), IME is the integrated mass enhancement of pixel, calculated as a sum over the N plume pixels as

$$IME = \frac{M}{N_A} \sum_{i}^{N} \Delta XCH_{4,i} VCD_{air,i} A_i, \quad \text{(S11)}$$

where $\Delta XCH_{4,i}$ is the enhancement of methane volume mixing ratio, calculated as

$$\Delta XCH_{4,i} = XCH_{4,plume,i} - XCH_{4,bg} \quad \text{(S12)}$$

where $XCH_{4,plume,i}$ is the methane mixing ratio for plume pixel i and $XCH_{4,bg}$ for the background, calculated using a local median filter (V aron et al., 2018). M is the methane molar mass (kg/mol), N_A is Avogadro's number (molec/mol), $VCD_{air,i}$ is the dry air column density (molec/m^2) derived from ERA5 air pressure and humidity profiles. A_i is the area of the geolocated ground pixel i. l is the plume length, derived as the square root of the square root of the plume mask area (Bruno et al., 2024). $u_{eff}$is the effective wind speed, and effectively the rate of turbulent diffusion.

The L4 uncertainty is estimated using Gaussian error propagation of Equation (S10), assuming uncorrelated errors, as follows:

$$\sigma_\phi = \sqrt{{\sigma_u}^2 + {\sigma_{\Delta XCH_4}}^2 + {\sigma_{VCD}}^2} \quad \text{(S13)}$$

σ_ϕ is the flux uncertainty (1 standard deviation, STD in kgCH$_4$/h), σ_u is the flux uncertainty attributed to the effective wind speed (i.e., plume speed). A fixed uncertainty of 0.21 m/s was assumed for ERA5 wind speeds (Giusti, 2022), representing the combined effects of model and representation errors at the spatial and temporal resolution of the ERA5 data. $\sigma_{\Delta XCH_4}$ is the flux uncertainty from the gas enhancement uncertainty (radiometric contribution), σ_{vcd} is the flux uncertainty caused by the uncertainty of the dry air column density. These contributions are computed as follows.

$$\sigma_u = \frac{m \Delta u}{l} \sum_{i}^{N} \Delta XCH_{4,i} VCD_{air,i} A_i, \quad \text{(S14)}$$

where m is the mass per molecule, $m = \frac{M}{N_A}$, l is the plume length, Δu is the plume speed uncertainty (in m/s), A_i is the area of plume pixel i calculated from the geolocation data.

$$\sigma_{\Delta XCH_4} = \frac{mu}{l} \sqrt{\sum_{i}^{N} \left(\sigma_{\Delta XCH_{4,i}} VCD_{air,i} A_i \right)^2}, \quad \text{(S15)}$$

Where $\sigma_{\Delta XCH_{4,i}}$ depicts the per pixel uncertainty (1 STD) of the methane enhancement. Assuming uncorrelated errors, it is currently calculated as $\sigma_{\Delta XCH_{4,i}} \approx \sqrt{2}\sigma_{XCH_4}$, where $\sigma_{XCH_{4,i}}$ is the L2 precision of pixel i, derived from the diagonal elements of the data least square covariance matrix.

$$\sigma_{VCD} = \frac{mu}{l} \sqrt{\sum_{i}^{N} \left(\sigma_{VCD_{air,i}} \Delta XCH_{4,i} A_i \right)^2}, \quad \text{(S16)}$$

where $\sigma_{vcd_{air,i}}$ is the uncertainty of the dry air column number density. To estimate the contribution of the dry air number density the ideal gas law, used to compute the dry air number density, was error propagated. The contribution to the flux uncertainty was found to be negligible compared to the release rate (< 100 g/h). The contribution from plume length uncertainty σ_l is ignored here, as it was found that l correlates with IME.

To assess if the L4 uncertainty from error propagation (Equation (S13)) is reasonable, in particular, assuming uncorrelated errors, although IME may correlate with plume length, Monte Carlo (MC) simulations were performed. From a given L2 result, for each pixel, a number of random noise samples (1000) were drawn from a normal distribution, characterised by the retrieved CH_4 as mean and its corresponding retrieval precision $\sigma_{XCH_4,i}$ as standard deviation. The resulting XCH_4 images were passed to the L3 and L4 processors to retrieve plume mask and flux, preserving all empirical correlations. The wind speed has been kept fixed using the actual measured value from the met station, so plume speed uncertainty did not contribute. Averaged over the overpasses, the STD/mean of the MC simulations is 31%, accounting for radiometric uncertainty and the plume length uncertainty, and is comparable to the average radiometric contribution (Equation (S15)) of 32%. This suggests that Equation (S13), although ignoring plume length uncertainty, does not underestimate or overestimate L4 uncertainty. An example MC result is shown in Figure S5 for overpass 904-950 on 16/6/2025 (Figure 7), with a mean flux of 162 ± 52 $kgCH_4/h$ (32% STD/mean). The mean uncertainty over all 1000 realisations is 122 $kgCH_4/h$ and comparable to the analytically derived uncertainty of 114 $kgCH_4/h$ from Equation S13.

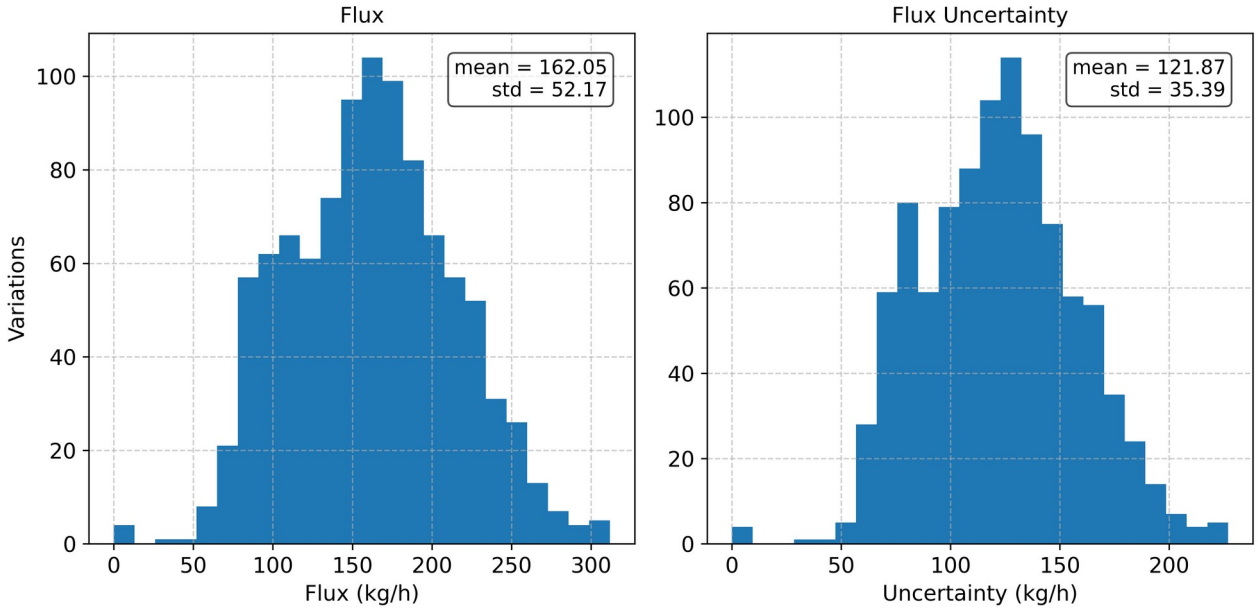

Figure S5. *Monte Carlo result for overpass 904-950 on 16/6/2025. Shown is the distribution of simulated L4 values with mean and STD used to assess L4 uncertainty from error propagation. Also*

shown is the distribution of the uncertainty from error propagation.